Cell Metabolism

Technology

SCENITH: A Flow Cytometry-Based Method to Functionally Profile Energy Metabolism with Single-Cell Resolution

Arguello et al., 2020, Cell Metabolism€
32, 1063–1075 December 1, 2020 ª

https://doi.org/10.1016/j.cmet.2020.11.007

Graphical Abstract

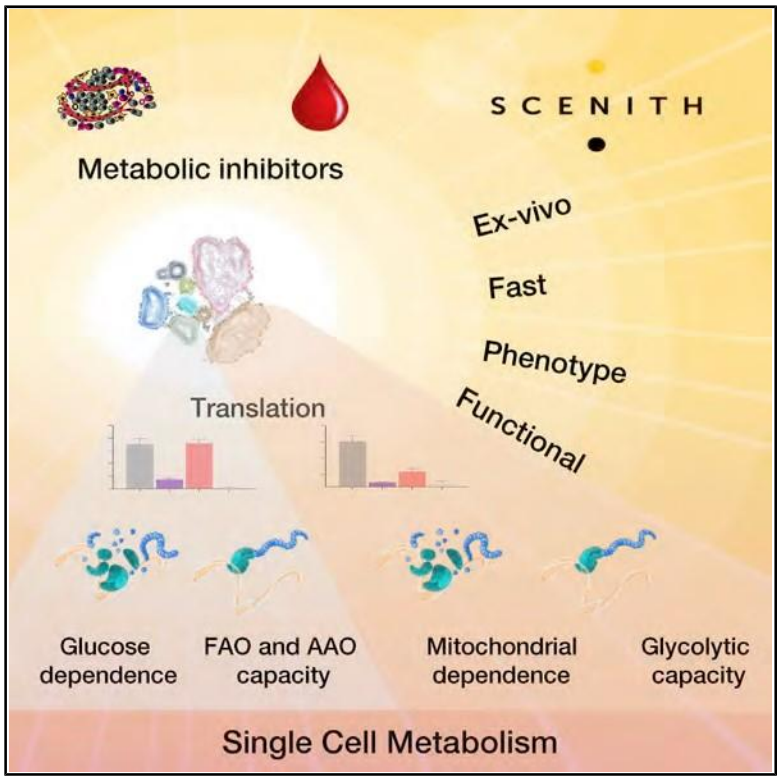

Highlights

- SCENITH is a simple method for complex metabolic profiling samples ex vivo
- SCENITH monitors rapid changes in protein translation upon metabolic pathway inhibition
- The profile of translation inhibition reveals metabolic capacities and dependencies
- SCENITH profiles abundant and non-abundant cells in parallel in blood and tumor samples

Authors

Rafael J. Arguello, Alexis J. Combes,€ Remy Char, ..., Emeline Tabouret, Matthew F. Krummel, Philippe Pierre

Correspondence

arguello@ciml.univ-mrs.fr

In Brief

Arguello et al. have developed a€ functional assay to quantify metabolic dependencies and capacities of multiple cell types with single-cell resolution in parallel. Applying SCENITH directly to whole blood and human tumor samples, they identify metabolic differences between tumor- and juxta-tumorassociated immune cells.

INTRODUCTION
Cell Metabolism

Technology

SCENITH: A Flow Cytometry-Based Method to Functionally Profile Energy Metabolism with Single-Cell Resolution

Rafael J. Arguello,€ [1,9,11,*] Alexis J. Combes,[2,3,9] Remy Char,[1] Julien-Paul Gigan,[1] Ania I. Baaziz,[1] Evens Bousiquot,[1] Voahirana Camosseto,[1,7] Bushra Samad,[2,3] Jessica Tsui,[2,3] Peter Yan,[2,3] Sebastien Boissonneau,[4] Dominique Figarella-Branger,[5] Evelina Gatti,[1,7,8] Emeline Tabouret,[6] Matthew F. Krummel,[2,3,10] and Philippe Pierre[1,7,8,10]

[1]Aix Marseille Univ, CNRS, INSERM, CIML, Centre d'Immunologie de Marseille-Luminy, Marseille, France

[2]Department of Pathology, University of California, San Francisco, San Francisco, CA, USA

[3]ImmunoX Initiative, University of California, San Francisco, San Francisco, CA, USA

[4]Aix-Marseille Univ, Institut de Neurosciences des Systems, Faculte´ de Medecine, Marseille, France

[5]Aix-Marseille Univ, APHM, CNRS, INP, Inst Neurophysiopathol, CHU Timone, Service d'Anatomie Pathologique et de Neuropathologie, Marseille, France

[6]Aix-Marseille Univ, APHM, CNRS, INP, Inst Neurophysiopathol, CHU Timone, Service de Neurooncologie, Marseille, France

[7]Institute for Research in Biomedicine (iBiMED) and Ilidio Pinho Foundation, Department of Medical Sciences, University of Aveiro, 3810-193 Aveiro, Portugal

[8]International Associated Laboratory (LIA) CNRS ''Mistra'', 13288 Marseille Cedex 9, France

[9]These authors contributed equally

[10]These authors contributed equally

[11]Lead Contact

*Correspondence: arguello@ciml.univ-mrs.fr https://doi.org/10.1016/j.cmet.2020.11.007

SUMMARY

Energetic metabolism reprogramming is critical for cancer and immune responses. Current methods to functionally profile the global metabolic capacities and dependencies of cells are performed in bulk. We designed a simple method for complex metabolic profiling called SCENITH, for single-cell energetic metabolism by profiling translation inhibition. SCENITH allows for the study of metabolic responses in multiple cell types in parallel by flow cytometry. SCENITH is designed to perform metabolic studies ex vivo, particularly for rare cells in whole blood samples, avoiding metabolic biases introduced by culture media. We analyzed myeloid cells in solid tumors from patients and identified variable metabolic profiles, in ways that are not linked to their lineage or their activation phenotype. SCENITH's ability to reveal global metabolic functions and determine complex and linked immune-phenotypes in rare cell subpopulations will contribute to the information needed for evaluating therapeutic responses or patient stratification.

Energetic metabolism comprises a series of interconnected biochemical pathways capable of using energy-rich molecules to produce ATP. Cells can produce ATP either by oxidative phosphorylation (OXPHOS) or by performing glycolysis. Aerobic glycolysis supports not only proliferation but also cell survival in hypoxic conditions. Immune cells are specially equipped to migrate into peripheral tissues and to adapt to the change in microenvironment. Their energetic metabolism profile is known to correlate with their microanatomical localization, activation, proliferation, or functional state (O'Sullivan et al., 2019; Russell et al., 2019). Activation of T cells is generally linked to a metabolic switch from OXPHOS to aerobic glycolysis (Pearce et al., 2009; Roos and Loos, 1973; Warburg et al., 1958; Wieman et al., 2007).

Competition for glucose within the tumor microenvironment influences cancer progression and the anti-tumoral immune response by regulating metabolism and function in both tumoral cells and tumor-infiltrating lymphocytes (TILs) (Chang et al., 2015). The presence of effector immune cells in the target tissue is a predictive marker of response to cancer immunotherapy (Galon et al., 2006). The success of immunotherapies is restricted to a relatively small proportion of patients, as it requires a functional and metabolically competent immune system to respond to treatment (Antonia et al., 2018; Wolchok et al., 2017). Consequently, there is a great need for a simple immuno-metabolic profiling method for complex samples that can be utilized to stratify patients before treatment and to monitor responses after immunotherapies.

Current methods to determine metabolic profiles can be classified into three groups. The first group,

epitomized by Seahorse (Agilent Technologies), uses metabolic inhibitors (i.e., 2-deoxyd-glucose [DG] and oligomycin A [O]) while monitoring the extracellular acidification rate (ECAR) and oxygen consumption rate

Cell Metabolism 32, 1063–1075, December 1, 2020 ª 2020 Elsevier Inc.

Table 1. Comparative Table of Methods to Profile Metabolism

Method	CyTOF (e.g., Met-Flow, scMEP)	MSI	Seahorse	SCENITH
Output	metabolic phenotype	metabolomic profile (unbiased)	metabolic capacities and dependencies	metabolic capacities and dependencies
Functional profile of the cells (no. of treatments)	no	no	yes (4)	yes (non-limited)
Cell purification required	no	no	yes	no
Single-cell resolution	yes	yes	no	yes
Phenotypic analysis	yes	no	no	yes
Compatible with cell sorting	no	no	no	yes[a]
Ex vivo application	yes	yes	no	yes
Metabolic readout	levels of markers (min 10 channels)	metabolite levels	changes in extracellular pH and [O_2]	changes in protein synthesis levels (one channel)
Time (Hs) from sampling to profiling	0–1	0–1	24	0–1
No. cells required in subsets	500	200	1,000,000	2,000
Equipment needed	CyTOF cytometer	any imaging mass cytometer	Seahorse Analyzer	any flow cytometer[b]

[a] Not shown

[b] SCENITH also has the potential to be analyzed by CyTOF. MSI, microscopy using heavy metal coupled with oligonucleotide-labeled antibodies (not shown).

(OCR). This method requires a large amount of purified cells to be incubated with special culture media for several hours and allows the user to establish different parameters and to determine global metabolic dependencies and capacities of the cells (Zhang et al., 2012). The second group quantifies the maximal activities of enzymes, such as the maximal dehydrogenase activity, by adding high concentrations of substrates to single cells using histochemistry (Miller et al., 2017) or to cell lysates. Finally, the third group uses mass spectrometry (MS) and MS imaging to measure the levels of metabolites produced by metabolic pathways (Palmer et al., 2017). Recently, three cytometry-based (FACS and CyTOF) phenotypic characterizations of cells, using a panel of anti-human or mouse antibodies recognizing transporters and metabolic enzymes, have been used in parallel with histology to correlate their expression with the microanatomical localization of T cells (Ahl et al., 2020; Hartmann et al., 2020; Levine et al., 2020).

Cell sorting and incubation with cell culture media can change the metabolic activity of the cells (Llufrio et al., 2018), and thus they cannot be applied to establish metabolic profiles of heterogenous and scarce living cell populations obtained from human blood samples or biopsies, ex vivo (Tables 1 and S1). Predicting the state of global metabolism by phenotyping the level of certain metabolic markers (Ahl et al., 2020; Hartmann et al., 2020; Levine et al., 2020; Wculek et al., 2019) or characterizing the maximal potential activity of a small subset of enzymes in situ (Miller et al., 2017) is very challenging. We aimed to complement the toolbox for metabolic studies in the single-cell era (Artyomov and Van den Bossche, 2020) by developing a method that functionally determines the overall metabolic capacities and dependencies of cells independent of their phenotype.

Approximatively half of the total energy that mammalian cells produce by degrading glucose, amino acids, and/or lipids is immediately consumed by the protein synthesis (PS) machinery (Buttgereit and Brand, 1995; Lindqvist et al., 2018; Schimmel, 1993). The tremendous energetic cost associated with this essential metabolic process offers a methodological opportunity to determine the PS levels as a measure of global metabolic activity. We took advantage of the drug puromycin (puro), whose incorporation is a reliable readout for measuring PS levels in vitro and in vivo (Andrews and Tata, 1971; Aviner, 2020; Hidalgo San Jose and Signer, 2019; Miyamoto-Sato et al., 2000; Nemoto et al., 1999; Rangaraju et al., 2019; Schmidt et al., 2009; Seedhom et al., 2016; Wool and Kurihara, 1967), combined with a novel antipuro monoclonal antibody, to develop a simple method for complex metabolic profiling with single-cell resolution based on PS levels as the readout. We termed this method SCENITH (singlecell energetic metabolism by profiling translation inhibition), with reference to our previous SUnSET (Schmidt et al., 2009) and SunRiSE (Arguello et al., 2018€) methods for studying protein synthesis. SCENITH was used directly in whole blood, in primary and secondary lymphoid organs, and in human tumor samples to deconvolve the complex functional energetics of immune and stromal cells with single-cell resolution. Our results demonstrate that our method is ideal for analyzing heterogenous

samples, from which the details of metabolism, particularly among rare immune cell subsets, have remained inaccessible.

DESIGN

Characterizing the Energetic Metabolism Profile by Monitoring Changes in Protein Synthesis Levels in Response to Metabolic Inhibitors

To test whether the kinetics of the levels of PS and ATP are tightly coupled, we measured in mouse embryonic fibroblasts (MEFs) both ATP and PS levels after blocking ATP production (Figure 1A).

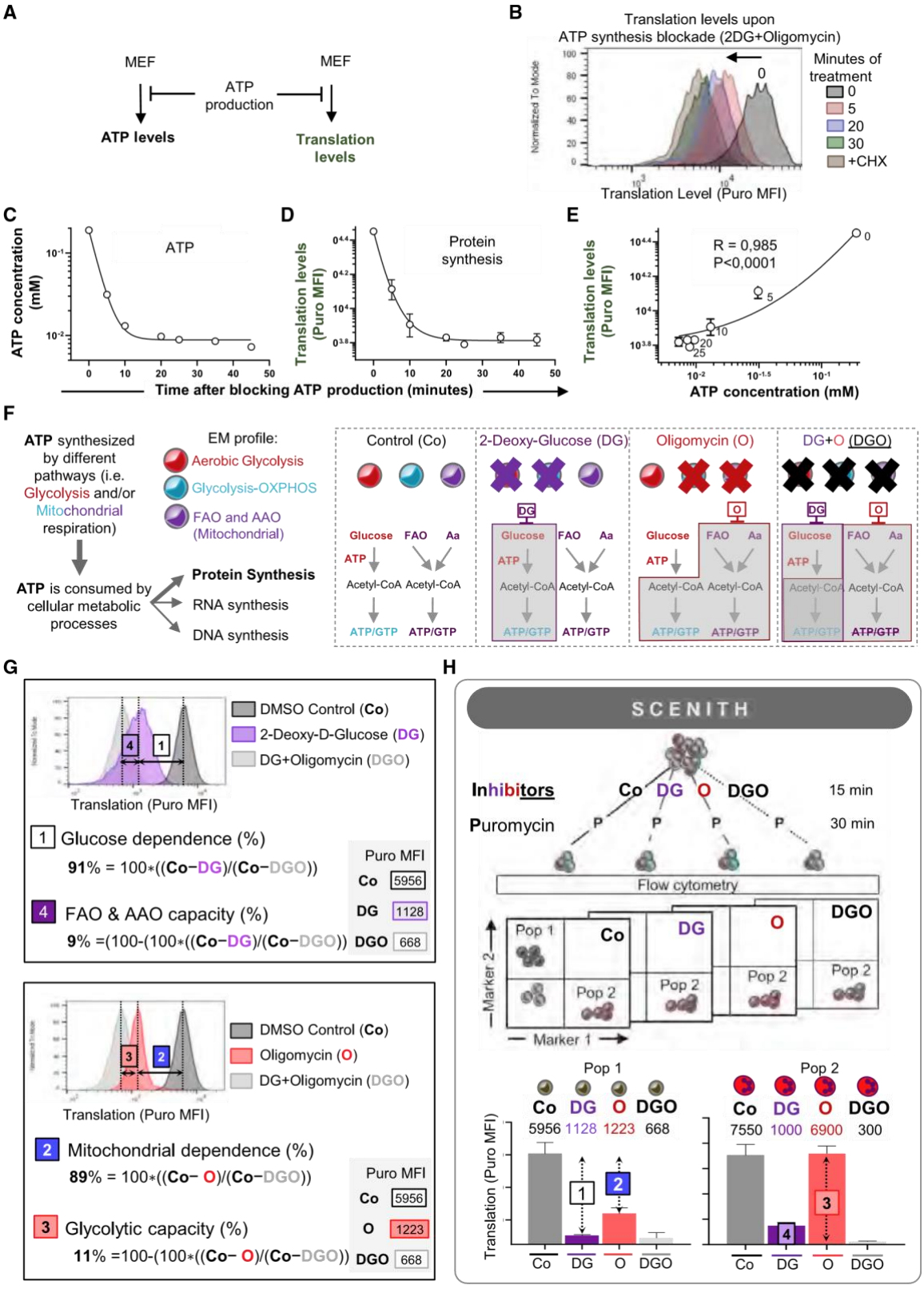

(legend on next page)

To inhibit ATP production, we treated cells with a mix of inhibitors that block both glycolysis and OXPHOS (Figure 1A). To optimize the signal-to-noise ratio of puro intracellular detection, we developed a novel monoclonal anti-puro antibody (clone R4743L-E8) specifically adapted for intracellular flow cytometry. Both PS levels (Figures 1B and 1D) and ATP levels (Figure 1C) dropped within 5–10 min after blocking ATP synthesis, with a strikingly similar slope, showing that changes in ATP levels and PS levels are tightly correlated (Figure 1E; $r = 0.985$; $p < 0.0001$). To increase the sensitivity of the translation measurement, the time of incubation with puro can be experimentally determined and increased if the cells of interest have very low metabolic activity (i.e., naive T cells) (Figure S1; Table S2). Indeed, we tested the optimal time of incubation for whole blood and determined that 40 min of puro treatment is optimal for detecting translation in T cells, monocytes, and neutrophils in whole-blood samples of mice (Figure S1C). To test the relationship between ATP consumption and transcriptional or translational activities, we treated metabolically active cells with the same inhibitors to block de novo ATP synthesis, together with translation and/or transcription inhibitors. Altogether, our results confirmed that PS is one of the most energy-consuming metabolic activities (Buttgereit and Brand, 1995; Lindqvist et al., 2018) (Figure S1), and most importantly, it represents a stable and reliable readout to rapidly evaluate the impact of metabolic pathway inhibition on the cell.

As both ATP and PS levels are tightly coupled, puro fluorescence (measuring PS) can act as a surrogate for energetic pathway inhibition and can be monitored by flow cytometry. The principle of SCENITH is thus to incubate a given sample in parallel with specific inhibitors of metabolic pathways. If a cell population is energetically dependent on the inhibited metabolic pathway, its ATP concentration will drop as well as its PS levels. The latter will be established using puro incorporation detected by direct immuno-fluorescence (Figures 1F and S1B). SCENITH allows metabolic profiles to be measured in heterogenous cell populations at single-cell resolution by combining cell identification and puromycinylation detection by multiparametric flow cytometry (FACS) (Figure 1G). Using PS levels, the level of glucose dependence is calculated to quantify the proportion of the PS, and therefore of ATP/GTP production, dependent on glucose oxidation (Figure 1F; STAR Methods). The mitochondrial dependence (mito dep), i.e., the proportion of PS dependent on OXPHOS, is similarly established. Two additional derived parameters, ''glycolytic capacity'' (Glyc. cap) and ''fatty acid and amino acid oxidation capacity'' (FAO and AAO cap), are also calculated. Glyc. cap is defined as the maximum capacity to sustain PS when mitochondrial OXPHOS is inhibited (Figure 1F; STAR Methods). Conversely, FAO and AAO cap is defined as the capacity to use fatty acids and amino acids as sources for ATP production when glucose oxidation is inhibited (i.e., glycolysis- and glucose-derived acetyl-CoA by OXPHOS) (Figures 1F and S1B).

RESULTS

SCENITH Recapitulates Seahorse Metabolic Profiling of Steady-State and Activated T Cells

The metabolic switch of T cells to aerobic glycolysis upon activation was originally documented in the 1970s (Roos and Loos, 1973; Warburg et al., 1958) and recently confirmed using the Seahorse technology (van der Windt et al., 2012, 2013). To benchmark our method, we monitored the energy metabolism in isolated human blood T cells at steady state or upon activation using Seahorse and SCENITH in parallel (Figure 2A). Upon activation, an increase in the glycolytic capacity of T cells was measured with both methods in excellent agreement (Figures 2B and 2C, respectively) (Spearman $r^2 = 0.85$, $p < 0.01$) (Figure 2D). We observed a statistically significant decrease in the spare respiratory capacity in bulk T cells upon activation with Seahorse (Figures S2A and S2B). Interestingly, an increase in OCR by Seahorse was paralleled with an increase in the global level of PS measured by SCENITH, albeit to a larger extent (Figures 2E and 2F, respectively). Overall, the metabolic profiles of T cells upon activation obtained by Seahorse and SCENITH were very consistent. The level of translation (Figure 2F) correlated with the global metabolic activity of the cells, and changes in the response to inhibitors confirmed the metabolic switch toward aerobic glycolysis that occurs upon T cell activation. However, SCENITH showed two main advantages over Seahorse measurements. First, the magnitude of the change in the glycolytic capacity and the standard error of the measurements with SCENITH were superior (Figures 2A, 2C, 2E, and 2F). Second, SCENITH analysis was performed with 10-fold fewer T cells. Moreover, SCENITH could incorporate a full spectrum of T cell markers in the analysis, allowing us to study in parallel the $CD3^+$ T cell subpopulations present in the bulk sample.

Metabolic Deconvolution of Blood T Cell Subsets by SCENITH Identifies a Memory $CD8^+$ T Cell Subset Constitutively Displaying High Glycolytic Capacity

We next applied SCENITH to mixed populations, which due to their heterogeneity are relatively inaccessible to metabolic monitoring by Seahorse. We took advantage of CD45RA, IL7RA

Figure 1. SCENITH Design Based on Dynamic Changes in Protein Synthesis Levels upon Blockade of Different Metabolic Pathways

(A) Blocking ATP production and kinetics of ATP and translation levels.

(B) Visualization of protein synthesis after puro incorporation and staining with a new monoclonal anti-puro (clone R4743L-E8). Histogram PS level by flowcytometry in MEFs after blocking both mitochondrial respiration and glucose oxidation for different amounts of time.

(C–E) Measurement in MEFs upon blocking ATP synthesis versus time of ATP levels (C), PS by flow cytometry (D), and correlation of both (E). Dot represents the means and bar the SD ($R = 0.985$, $p < 0.0001$, $N = 3$).

(F) Schematic representation of a sample that contains three cell types with different metabolism profiles (aerobic glycolysis, glycolysis/OXPHOS, FAO, and AAO/OXPHOS). Treating the mix of cells with specific drugs (DG or O) will affect each cell subset in a different way.

(G) Examples of metabolic monitoring using SCENITH. The glucose dependence and FAO and AAO capacity and the mitochondrial dependency and glycolyticcapacity can be calculated from the MFI of puro in the different treatments following the formulas (STAR Methods).

(H) Description of SCENITH procedure. Extract the sample, divide it, and treat each with the inhibitors (e.g., DG, O, DG+O, H) and puro. After staining and flowcytometry, the profile of response of the different cell subsets is analyzed. The profile reveals the metabolic capacities and dependencies of the cells (i.e., high glucose dependence [''pop 1''] and high glycolytic capacity profile [''pop 2'']).

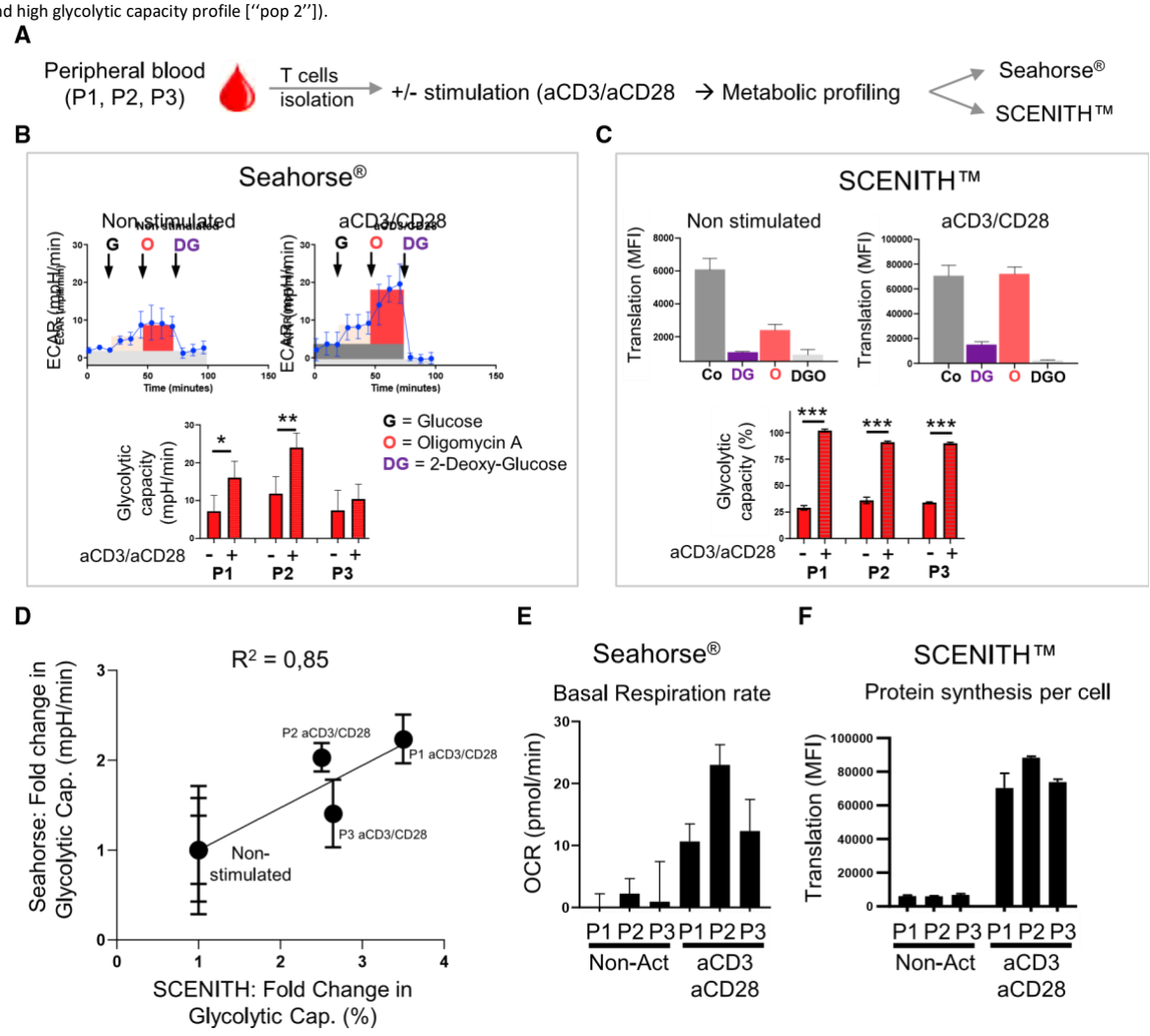

Figure 2. Parallel Seahorse and SCENITH Metabolic Analysis of Resting and Activated T Cells

(A) Scheme of the experiment for analysis of resting and activated T cells.

(B and C) Metabolic profile of T cells from three healthy donors (P1, P2, and P3) analyzed with Seahorse (B) and SCENITH (C). ECAR and translation levels of nonactivated and activated T cells (P1) and glycolytic capacity from both methods are shown (*$p < 0.05$; **$p < 0.01$; ***$p < 0.001$; N = 3 each in triplicate). (D) Correlation between the changes in glycolytic capacity of steady-state and activated T cells from three donors measured by Seahorse and SCENITH (Pearson $r = 0.92$; $R^2 = 0.85$; $p < 0.01$; N = 3).

(E) Basal OCR in non-activated (non-Act) and activated T cells. Each bar represents the mean of P1, P2, and P3 (in triplicate).

(F) Basal translation levels (anti-Puro gMFI) in non-activated (non-Act) and activated T cells (aCD3/CD28). Bars represent the mean of P1, P2, and P3. (G) SCENITH metabolic profile of whole blood directly treated with inhibitors with or without pre-incubation (1:4 V/V) in DMEM 10% FCS for 3 h. Data represent pooled whole blood from three mice (in duplicate) from three independent experiments. Two-way ANOVA, multiple comparisons.

(CD127), CCR7, CD45RO, CD57, PD1, and perforin expression to identify and analyze T cell subsets present in human blood draws. Briefly, naive T cells show expression of both CD45RA and IL-7 receptor alpha (CD127) and the chemokine receptor CCR7. The lack of expression of CD45RA is a known marker of antigenic stimulation experience (memory and effector cells). Early effector memory (EEM) $CD8^+$ T cells do not express CD45RA and CD57, and do not yet express cytotoxic markers like perforin. Monitoring the expression levels of these nine markers and analysis by dimensionality reduction, using tdistributed stochastic neighbor embedding (t-SNE), yielded six phenotypically distinct clusters/subpopulations (Figures 3A and 3B). The metabolic profiles of non-activated naive T cells, as well as memory (effector memory and central memory) $CD4^+$ and highly differentiated $CD8^+$ (HDE), showed a medium to high degree of mitochondrial dependence (Figure 3C), consistent with previous reports on their metabolic activity (Pearce et al., 2009). In contrast, the less abundant cell subsets such as EEM $CD8^+$ T and natural killer (NK) cells (a small fraction that co-purified with T cells) showed higher glycolytic capacity. To determine if similar metabolic trends are observed in other species and preparations, we performed SCENITH

on resting and activated mouse splenic T cells (Figures S3A and S3B) and human blood central memory CD4⁺ T cell subsets (Figure S3C). Our results consistently demonstrated a switch toward high glycolytic capacity and high glucose dependence in both

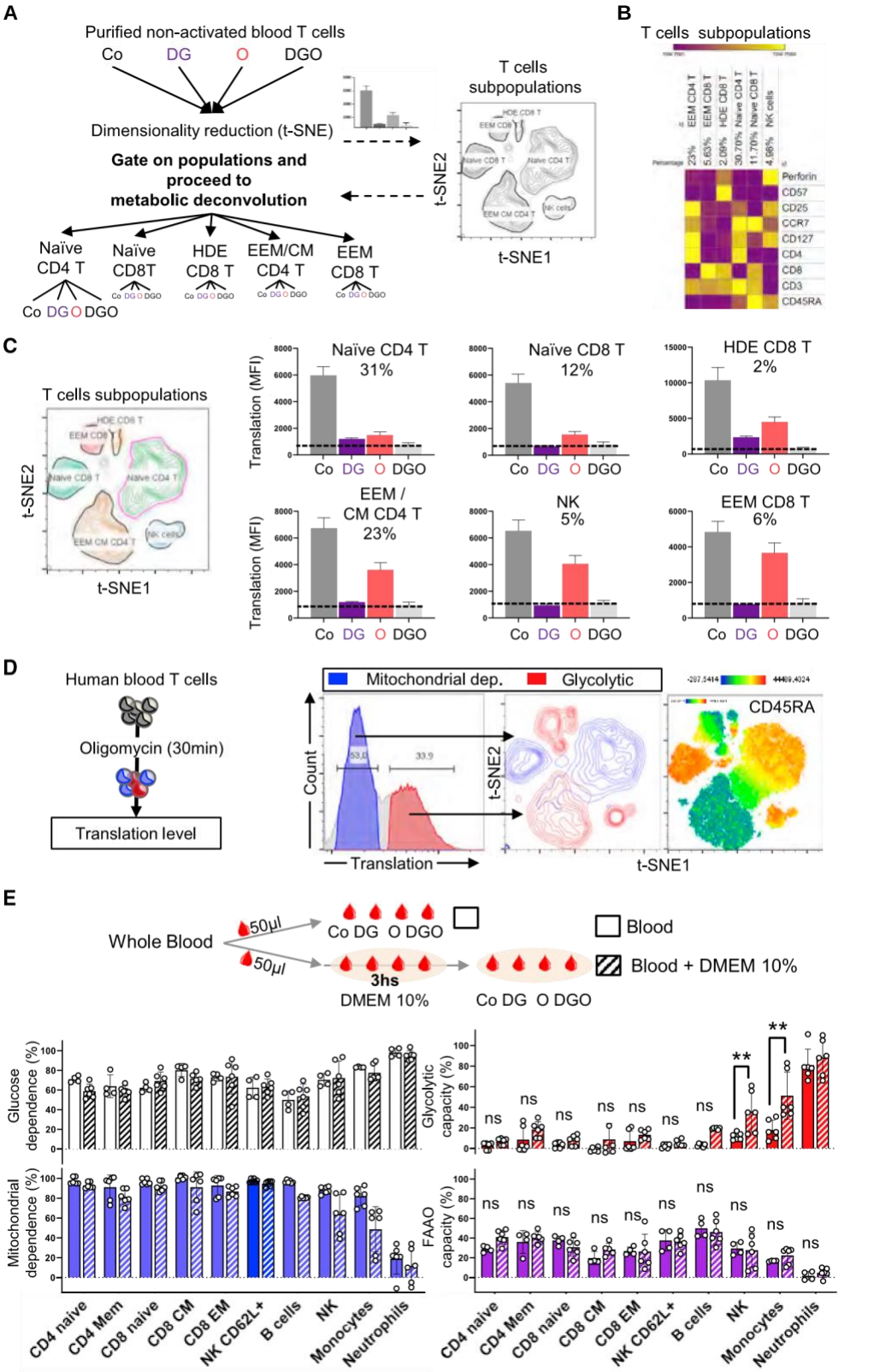

Figure360▷

Figure 3. Metabolism Profile of Resting Human Blood T Cells by SCENITH Identifies Different Metabolic Profile of Human T Cell Subsets

For a Figure360 author presentation of Figure 3, see https://doi.org/10.1016/j.cmet.2020.11.007.

(A) SCENITH analysis pipeline of T cells purified from human blood (95% pure). Dimensionality reduction (t-SNE) based on phenotypic markers is performed on the concatenated treated cells (Co, DG, O, and DGO).

(legend continued on next page)

mouse and human T cells upon activation (Figure S3). In bulk analysis, naive CD4$^+$ and CD8$^+$ T cells represented the most abundant subsets and thus likely dominated the energy metabolism monitoring performed by Seahorse (Figures 2E and 3C). Consequently, Seahorse measurements indicate a rather low ''mean'' glycolytic rate/capacity and high ''mean'' oxygen consumption rate (Figure 2B) and are thus in accordance with the metabolism of naive T cells determined by SCENITH (Figures 3C and 3D). However, the presence of CD8$^+$ EEM, which display high glycolytic capacity but represent no more that 5% of the T cells present in the sample (2,000 cells), remained completely masked during Seahorse analysis.

Another feature of SCENITH's resolutive power is the possibility to characterize single-cell behaviors according to their sensitivity to metabolic inhibitors independent of their phenotype. This allows for the identification of functional metabolic heterogeneity first, and for the determination of the phenotype or sorting cells afterward. As a proof of concept, resting purified T cells were treated with oligomycin prior to translation monitoring. The histogram of translation levels showed two T cell subpopulations upon mitochondrial inhibition, one with high and one with low levels of translation (Figure 3D). The population with blocked translation was labeled as ''mitochondrial dependent'' and the cells with a high level of translation were labeled as ''glycolytic'' (Figure 3D). As shown in the t-SNE, the phenotype of glycolytic and respiratory T cells recapitulated our previous results (Figures 3A–3C) and showed that the expression of CD45RA, mostly present in naive T cells, correlated well with the level of mitochondrial dependence (Figure 3D). In conclusion, we found that SCENITH allows for both the measurement of the metabolic profile of known non-abundant cell subsets of interest and the sorting and identification of ''unknown'' cells with specific metabolic dependencies present within a heterogenous sample.

Cellular energy metabolism is affected by nutrient availability, and Seahorse measurements typically require special unbuffered media and incubation in culture media over several hours. Comparatively, SCENITH can be performed directly on whole blood. To investigate the effect of media, we tested whether short-term incubation of blood with cell culture media would impact the metabolic profile of immune cells. Freshly isolated blood was directly treated with control, DG, O, or DGO and puro or treated after pre-dilution and incubation for 0 or 3 h in DMEM 10% FCS. Incubation of blood for 3 h with culture media induced a statistically significant increase in the glycolytic capacity of NK cells and monocytes (Figures 3E and S3D). In contrast, it had no impact on the metabolic parameters of both naive and effector CD4$^+$ and CD8$^+$ T cells, B cells, and neutrophils.

Metabolic Profiling of Mouse and Human Myeloid Cell Subsets

Compared to T cell subsets, the metabolic profile of myeloid cell subsets from human and mouse tissue origin has been far less studied (Saha et al., 2017). Among myeloid cell subsets, dendritic cells (i.e., DC1, DC2, DC3, and pDCs) are non-abundant professional antigen-presenting cells (APCs), which serve as sentinels for the immune system. Each subset expresses a particular set of microbial pattern recognition receptors and is specialized in activation of CD8$^+$ (i.e., DC1) and CD4$^+$ (i.e., DC2 and DC3) T cells and antiviral cytokine production (pDCs). For instance, lipopolysaccharide (LPS) detection by TLR4 on DC2 and DC3 results in changes in gene expression, membrane traffic, and energetic metabolism (Amiel et al., 2012; Everts et al., 2012; Krawczyk et al., 2010). DCs patrol all tissues emanating from the bloodstream, where they represent a very small fraction of the peripheral blood mononuclear cells (PBMCs), making the isolation of millions of DC1s, DC2s, or pDCs from the same donor very challenging. We therefore used SCENITH to profile the energy metabolism of human blood myeloid cell subsets from healthy donors as well as of mouse bone marrow- and spleen-derived DCs stimulated or not to generate a detailed metabolic atlas of the myeloid cell populations.

Following deconvolution, we first ranked myeloid cells by glucose dependence, finding that classical monocytes (Mono1, CD14$^+$CD16) were the most glucose dependent, whereas the DC precursors (DC5) were the least (Figure 4A). These populations lay near the extremes of mitochondrial dependence: DC5s display highest and Mono1 the lowest. However, we also observed examples of cell subsets (e.g., pDC and Mono2) that were dependent on glucose and mitochondrial respiration. In contrast, DC1 and DC2 displayed relatively high glycolytic capacity and moderate glucose dependence, suggesting a certain degree of metabolic plasticity. As expected, cells ranked in opposite order for FAO and AAO capacity compared to glucose dependence, consistent with the idea that cells with low glucose dependence can sustain translation and energy production by free fatty and/or amino acid oxidation.

To test whether a rapid metabolic switch occurs upon TLR4 activation in human myeloid cells, we used an antibody panel for analyzing Mono1, Mono2, DC1, DC2, and pDCs in PBMCs treated with LPS. While the Mono1 subset increased their global level of translation (Figure S4A) and the DC1 subset showed a mild increase in glucose dependence and a moderate decrease in mitochondrial dependence (Figure S4A), all other subsets did not change their metabolism.

We previously observed metabolic differences in human versus mouse blood monocytes. To gain insight into the

(B) Heatmap showing the level of expression of each marker (gMFI) in each cluster/subset from the t-SNE after dimensionality reduction.

(C) Metabolic profile of the T cell subsets identified (naive CD4 and CD8 T cells in green, memory CD4 and HDE CD8 T cells in orange, EEM CD8 T cells in red, andNK cells in blue) after SCENITH analysis. Representative translation level (anti-Puro gMFI) (P1) is shown (N = 3). Black line represents background level obtained after DG+O treatment.

(D) Two distinct metabolic profiles in human blood T cells after O treatment (left panel) revealing glycolytic and mitochondrial-dependent T cell subsets. Histogramshows the level of translation in all T cells (light gray line) upon mitochondrial inhibition, indicating the presence of glycolytic cell subsets (in red) and mitochondrialdependent cells

(in blue). Gating them into the t-SNE plot (right panel) to identify the phenotype of glycolytic and mitochondrial-dependent cells (blue). The marker of antigen experience CD45RA, lost in cells that have been previously exposed to TCR stimulations, correlates with the metabolic profile.

(E) Metabolic changes induced by short-term incubation of blood with cell culture media. Metabolic parameters of cell types when blood is pre-incubated withDMEM 10% FCS (0 or 3 h) or directly incubated with the inhibitors (i.e., Co, DG, O, DGO, or Harringtonine) and puro. Data from pooled whole blood from three mice (in duplicate) from three independent experiments are shown (N = 3). Statistical significance between both conditions by t test (**p < 0.005).

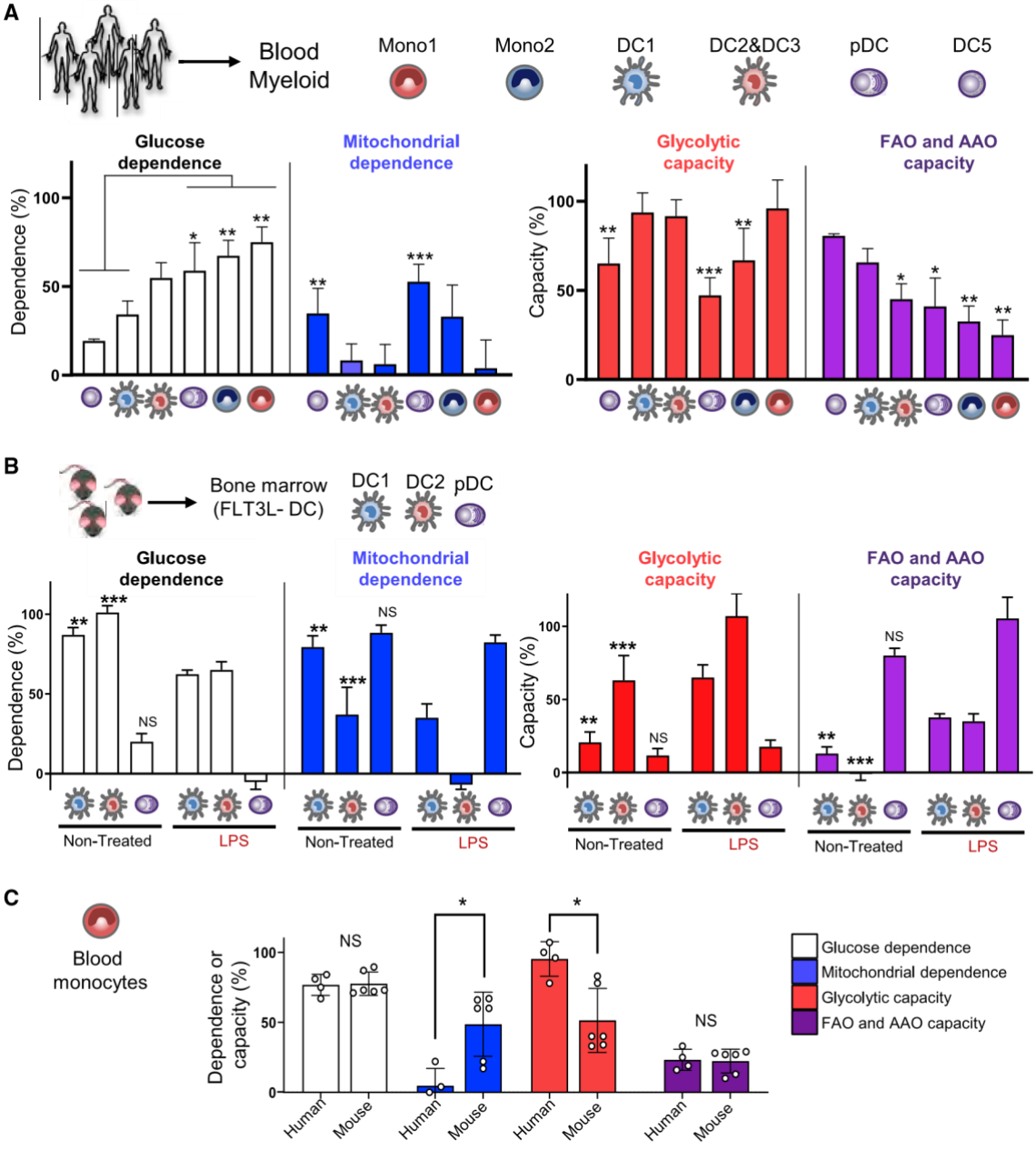

Figure 4. Metabolic Profile of Human Blood DCs and Monocytes and Mouse Bone Marrow-Derived DCs Using SCENITH

(A) Metabolic profile of human blood monocytes and DC subsets obtained by SCENITH (N = 5 independent healthy donors). Statistical significance by two-way ANOVA comparing all columns (*p < 0.05; **p < 0.005; ****p < 0.0001). The pDC, Mono2, or Mono1 showed statistically significant differences against DC1 or DC5. (B) Metabolic profile of mouse bone marrow-derived DCs (FLT3L-DC) obtained by SCENITH (N = 3) in non-treated versus LPS-treated cells; two-way ANOVA, *p < 0.05; **p < 0.005; ****p < 0.0001.

(C) Metabolic profile of blood monocytes from human (N = 4) or mouse (N = 9, 3 mice pooled, in duplicate, three independent experiments). Statistical significance between human and mouse monocytes by t test (*p < 0.05).

metabolic profile of mouse DC populations, we analyzed bone marrow-derived DC1, DC2, and pDC (FLT3L-BMDC) subsets at steady state and upon activation with LPS (Figure 4B). As in human samples,

the mouse DC2 subset showed the highest glycolytic capacity, followed by DC1 and pDC subsets. While glucose dependence was high in both DC1 and DC2 subsets from human (40% and 55%) and mouse (80 and 100%) samples, a 4-fold lower glucose dependence was observed in mouse versus human pDCs (15% versus 60%). LPS treatment shifted the DC1 and DC2 metabolic profiles toward lower mitochondrial dependence. However, only DC2 showed an increased global level of PS, probably reflecting the abundant TLR4 expression in this DC subset. Considering that we analyzed DCs isolated from human blood and derived in vitro from mouse bone marrow,

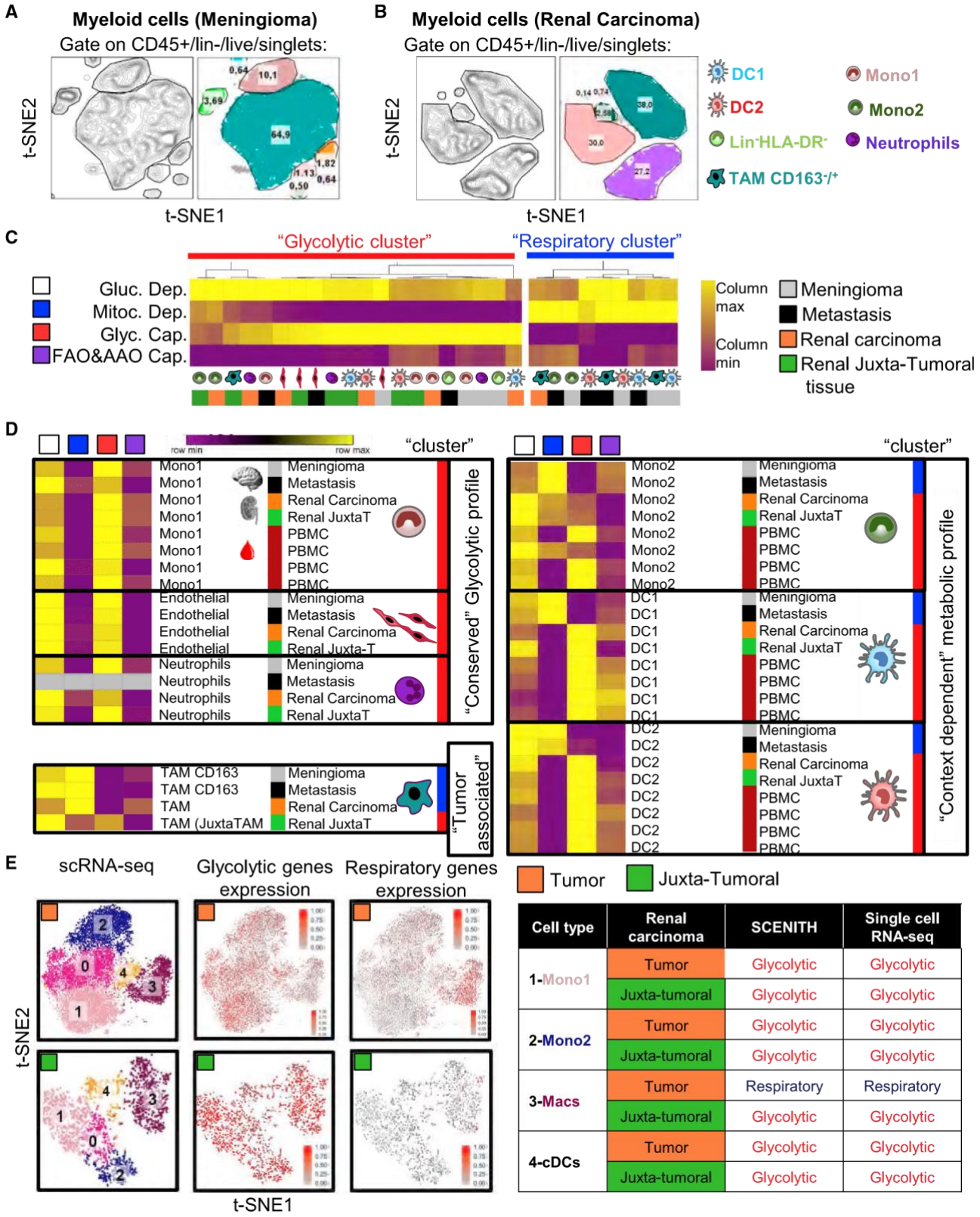

Cell type	Renal carcinoma	SCENITH	Single cell RNA-seq
1-Mono1	Tumor	Glycolytic	Glycolytic
	Juxta-tumoral	Glycolytic	Glycolytic
2-Mono2	Tumor	Glycolytic	Glycolytic
	Juxta-tumoral	Glycolytic	Glycolytic
3-Macs	Tumor	Respiratory	Respiratory
	Juxta-tumoral	Glycolytic	Glycolytic
4-cDCs	Tumor	Glycolytic	Glycolytic
	Juxta-tumoral	Glycolytic	Glycolytic

Figure 5. Paralleled SCENITH and scRNA-Seq in Human Tumor and Juxtatumoral Samples Identify Conserved Metabolic Profiles

(A and B) Myeloid subsets observed in the human meningioma tumor sample (A) and renal carcinoma (B). Myeloid cells gated on CD45$^+$/CD3CD20CD19CD56/Live-dead/singlets. Number in the t-SNE represents the percentage of the population.

(legend continued on next page)

their SCENITH metabolic profiles are surprisingly comparable. These results confirm that SCENITH allows the user to identify cell populations sharing similar metabolic profiles and that energy metabolism in DCs varies according to their state of activation.

Profiling the Metabolic State of Human TumorAssociated Myeloid Cells

Immunotherapies are a game changer in oncology, yet only a fraction of patients show complete immune-mediated rejection of the tumor. The heterogeneous responses of patients to immunotherapies have created a strong need for understanding the functional state of tumor-associated immune cells (Galon et al., 2006). We thus used SCENITH to perform parallel phenotypic and metabolic profiling of blood and tumor samples, and to investigate the heterogeneity of immune cell subsets by comparing tumors of diverse origins. In particular, we analyzed PBMCs from healthy donors, explanted meningioma, brain metastasis (originated from a breast cancer), and renal carcinoma tumors and renal juxta-tumoral tissue. In the case of kidney tissues, both SCENITH and single-cell RNA sequencing (scRNA-seq) analysis were performed in parallel on the same samples.

We observed eight myeloid subsets in meningioma and six in renal carcinoma, in which the phenotype and metabolic profile were determined (Figures 5A–5C, S5A, and S5B). Upon clustering of all the cell subsets in all tumors based on their metabolic profile, two groups emerged, a ''glycolytic cluster'' and a ''respiratory cluster'' (Figures 5C and S5C). Mono1 and neutrophils displayed glycolytic metabolism profiles in all blood samples and tumors tested (Figure 5D). In contrast, Mono2, DC1, and DC2 showed relatively high glycolytic capacity when isolated from kidney tumor and juxta-tumoral tissues, while these subsets showed high respiratory metabolism profile in the two brain tumors. Conversely, tumor-associated macrophages (TAMs) showed high mitochondrial dependence, while juxta-tumoral macrophages displayed higher glycolytic capacity (Figure 5D), suggesting that the tumor microenvironment modifies TAM metabolism. The decrease in the glycolytic capacity in TAMs as compared to juxta-tumoral macrophages was previously associated with increased immunosuppression, tumor progression, and poor patient survival (Vitale et al., 2019). These SCENITH results reveal that the anatomical origin of the tumor could influence the metabolism of immune subsets, introducing an additional layer of heterogeneity in the tumor environment.

Linking scRNA-Seq and Energetic Metabolism Profile in Tumor-Associated Myeloid Cells

We decided to link the discriminative power of SCENITH with scRNA-seq to support our results regarding the cellular complexity of the renal carcinoma tumor environment and to correlate metabolic profiling with gene expression. We compared the functional metabolic profile obtained by SCENITH with the metabolic gene expression pattern obtained by scRNAseq. We first identified expression signatures of glycolytic and respiratory genes that tightly correlated with the functional metabolism profiles of human blood myeloid cells (Figure S5D). Then, we tested the expression (mRNA) of these glycolytic and respiratory metabolic genes in the tumor-associated myeloid populations (CD45$^+$LinHLA-DR$^+$). Sorted cells from the renal carcinoma and juxta-tumoral tissue were subjected to scRNA-seq (Figures 5E and S5E). Analysis of 12,801 and 2,080 cells for the tumor and for the juxta-tumoral tissue yielded 6 and 5 clusters, respectively. To rigorously identify the populations, we used well-known signatures (Villani et al., 2017) and numbered cellular identities in the t-SNE representations (Figure S5E). We focused on 5 Mono/Mac clusters expressing MAFB and/or CSF1R that were present in both tumor and juxta-tumoral tissue (Figure S5F). Expression of classical surface markers such as CD16 and CD14 (Figure S5G) confirmed that clusters 0 and 1 represent classical monocytes (Mono1). Cluster 2 represents CD14CD16$^+$ nonclassical monocytes (Mono2), while co-expression of CD14 and CD16 for clusters 3 and 4 corresponds to macrophagelike populations. We performed unsupervised differential gene expression (DGE) analysis and generated heatmaps for the top 5 most differentially expressed in the tumor (Figure S6A, left) and the juxta-tumoral tissue (Figure S6A, right). In addition to highlighting key genes that contributed to the unbiased segregation of these populations in both tissues, we confirmed the high expression of macrophage-specific genes by clusters 3 and 4, such as APOE, C1QC, and RGS1. We next overlaid the t-SNE plots with our two metabolic gene signatures. Highly correlating with SCENITH profiles, monocyte clusters (0, 1, and 2) presented an enrichment in glycolytic gene signature both in tumor and juxta-tumoral tissue. Conversely, macrophages (cluster 3) showed high expression of the respiratory signature in the tumor, while, as predicted by SCENITH, this was not detectable in juxtatumoral tissue (Figure 5E). DCs, distinct from macrophages, presented an enrichment in a glycolytic gene signature both in tumor and juxta-tumoral tissue (Figure S6B).

Altogether, these results indicate that tumor micro-environment specifically modifies the functional metabolism of macrophages by durably affecting metabolic gene expression. By correlating the results of scRNA-seq analysis and SCENITH profiling on blood myeloid cell subsets (Figure 5F), we identified a functional gene signature (Figure S5D) that can be used to describe the metabolic profile using gene expression.

DISCUSSION

SCENITH is a simple method for complex immuno-metabolic profiling. It allows the user to simultaneously establish the phenotype and extract the global metabolic profile of multiple cell types in parallel, ex vivo. This rapid and sensitive method is consistent and comparable to other established techniques, including Seahorse. As the treatments with inhibitory drugs are performed in parallel, SCENITH can be used to monitor cellular responses to a combination of multiple metabolites and inhibitors. Given that flow cytometers are available in most research institutes and hospitals, SCENITH represents an accessible method to study energy metabolism. Compared to other methods (Tables 1 and S1), its sensitivity, accessibility, singlecell resolution, requirement for only one fluorescent channel, stability of the readout, manipulation time, compatibility with fixation, and sorting make SCENITH an unrivalled approach for studying global metabolism in cells in tissue slices and complex populations ex vivo (Artyomov and Van den Bossche, 2020).

The resolutive power of SCENITH highlighted variations among subsets of the same cell populations. Our results suggest that changes in metabolism are embedded in the myeloid differentiation program and that modulating metabolism in DC precursors might influence the generation of DC subsets with potential clinical relevance. One surprising observation is the higher glycolytic capacity of human blood monocytes compared to the mouse blood counterpart (Figure 4C). This may be an inherent difference between human and mouse, or influenced by environmental factors, like circadian rhythms, diet, and/or microbiota, and other factors. Interestingly, mouse monocytes increased their glycolytic capacity upon incubation with cell culture media, suggesting that the metabolic profile of these cells is sensitive to nutrient availability.

It has been previously shown by Marciano et al. that puromycinylation does not reveal a very strong decrease in PS levels in cell lines under mild conditions of starvation. This evidence led the authors to conclude that puro is not reliable to monitor translation in cells upon starvation conditions. In contrast, we could reliably detect inhibition of PS upon treatment with metabolic inhibitors, reaching levels of inhibition (i.e., DGO) comparable to the treatment with an inhibitor of translation initiation (Figure S3D). The results from Marciano et al. and our study might be interpreted as contradictory; however, the experimental conditions of both studies are not comparable, the main difference being that they pulse cells with puro only after 3 h of mild starvation and at this late time point cell lines might be simply recovering translation to some extent.

The metabolic profile of immune subsets in the blood correlates with migratory capacity and effector functions in the body. Neutrophils and monocytes migrate into hypoxic/ damaged tissues and are already engaged in aerobic glycolysis in the blood. We confirmed this in human monocytes and neutrophils in the blood and within the tumor. In a similar fashion, the metabolic profile of naive and effector CD8 T cell subsets supports the idea that the metabolic profile of cells in the blood is pre-adapted and related to the migratory capacity and function of the cells. This hypothesis will require further studies that may profit from SCENITH.

(C) Heatmap of the metabolic profile (columns) of each myeloid cell subset from each type of tissue (rows). Unsupervised hierarchal clustering of subsets bymetabolic profile identifies respiratory (blue bar) and glycolytic (red bar) clusters.
(D) Reordering of the rows by cell type based on (B) to identify changes in metabolism profile in the same cell subset in blood, tumors, and juxta-tumoral tissue.(E) Clusters of myeloid cells identified in the renal carcinoma and juxta-tumoral tissue by scRNA-seq (left panel). Expression of glycolytic and respiratory gene signatures in all cells extracted from the tumor. Summary of the results obtained by SCENITH and scRNA-seq in tumor and juxta-tumoral myeloid cells. Populations named with numbers in the t-SNE and described in table.

Importantly, SCENITH can establish the metabolic profile of circulating EEM CD8 T cells directly from 200 mL blood. EEM CD8 T cells represent around 5% of the total T cells (i.e., 500 cells per condition), and we consistently measured their metabolic profile. Of note, the same analysis would have required the purification of 1.2 million EEM (400,000 EEM in triplicates) to be analyzed with the Seahorse XF24, thus representing a gain of sensitivity of approximately 800-fold. This gain was even more dramatic when the metabolism profile of DC subsets was established from human tumor biopsies, in which they constituted approximately 0.5% of the myeloid cell population. These results demonstrate the analytical capacity and discriminative power of SCENITH and its potential in analyzing how the diet, age, and anatomical/tissue context could influence energetic metabolism of immune cell subsets. The metabolic profile of innate and adaptive immune cells correlates with the type of cytokines they produce; thus, the metabolic profile represents a universal readout for functional state (Buck et al., 2015). For these reasons, SCENITH analysis could be used to define the immune metabolic contexture and complement an immunoscore that defines immune fitness of tumors and predicts and stratifies patients for tailored therapies, aiming to manipulate metabolic pathways to improve anti-tumoral immune effector functions.

Limitations of Study

As a consequence of having single-cell resolution, SCENITH does not amplify the signal by increasing the number of total cells analyzed. For this reason, one of the limitations of our method is that it is not suitable for studying cells with undetectable levels of PS (i.e., mature spermatozoids, quiescent stem cells, acutely stressed cells, etc.). Of note, the incubation time with inhibitors and puro can be increased when cells with very low metabolic activity are studied (i.e., circulating naive T cells and others) (Figure S1C; Table S2). Another limitation of SCENITH is that at steady state we assess one metabolic readout (i.e., the global level of PS). However, SCENITH may potentially be combined with a larger panel of phenotypic markers, fluorescent lipids or sugars, and mitochondrial tracers. These additions will need to be properly tested to ensure that they do not interfere with the metabolic functions of the cells.

SCENITH is based on a fixable readout detected by immunohistology, and we envision the combination of our method with ATAC-seq, Cite-seq, CyTOF, and MS imaging ex vivo and potentially also in vivo (Tables 1 and S1). One limitation when

combining SCENITH with sequencing technologies is that fixation and permeabilization are required for staining with antipuro. For this reason, the scRNA-seq, ATAC-seq, or imaging method to be used needs to be compatible with this treatment (Attar et al., 2018; Rosenberg et al., 2018).

Translation levels by puromycinylation can be determined in vivo (Hidalgo San Jose and Signer, 2019; Seedhom et al., 2016). However, performing SCENITH in vivo has been until now challenging, in particular with regard to determining the time of treatment and concentrations of the inhibitors to ensure homogeneous distribution throughout the different tissues of a whole animal (e.g., 2-DG is rapidly excreted, and puro does not cross the blood-brain barrier). The implementation of SCENITH in vivo will require further investigation; however, we show here that SCENITH can be efficiently applied to fresh whole blood (Figures S1 and 3E) and in fresh tissue slices (Figure 5), avoiding interferences coming from cell culture conditions or cell isolation procedures. Our method allowed us to reveal the global metabolic capacities and dependencies of multiple cell types in parallel within their physiological context (i.e., physiological concentration of metabolites, growth factors, electrolytes, and cellular interactions).

STAR+METHODS

Detailed methods are provided in the online version of this paper and include the following:

- d KEY RESOURCES TABLE d
- RESOURCE AVAILABILITY
  - B Lead Contact
  - B Materials Availability
  - B Data and Code Availability d EXPERIMENTAL MODEL
- AND SUBJECT DETAILS
  - B Mouse Experiments
  - B Human Experiments
  - B Cell Lines d
- METHOD DETAILS
  - B ATP Measurement
  - B Metabolic Flux Analysis (Seahorse)
  - B SCENITH
  - B Processing of Human Solid Tumors SCENITH
  - B Human Single Cell RNA-sequencing
  - B Single Cell Data Processing
  - B Cellular Identification and Clustering of scRNaseq data d
- QUANTIFICATION AND STATISTICAL ANALYSIS
  - B Statistical Analysis
  - B Quantification and Meaning of SCENITH Derived Parameters

SUPPLEMENTAL INFORMATION

Supplemental Information can be found online at https://doi.org/10.1016/j.cmet.2020.11.007.

ACKNOWLEDGMENTS

The project was supported by Contrats Proof of Concept CoPoc 2019 INSERM ''ZIPT R19011AS'' to R.J.A., Mobilite´ Grant Cance´ ropoˆ le (to UCSF) to R.J.A., and the Cance´ ropoˆ le PACA ''Emergence'' grant ''HiDi-Glio'' to R.J.A. This study was partly supported by research funding from the Canceropoˆ le PACA, Institut National du Cancer, and Re´ gion Sud to R.J.A. The P.P. laboratory is sponsored by la Fondation de la Recherche Me´ dicale (FRM) grant DEQ20140329536. The study was partly supported by grants from l'Agence Nationale de la Recherche (ANR-FCT 12-ISV3-0002-01), A*MIDEX project ''CSI'' (ANR-11-IDEX-0001-02), DCBIOL Labex (ANR-11-LABEX-0043), INFORM Labex (ANR-11-LABEX-0054) funded by the ''Investissements d'Avenir'' French government program, the Ilı´dio Pinho Foundation, FCT (Fundac¸ a˜ o para a Cieˆ ncia e a Tecnologia), and Programa Operacional Competitividade e Internacionalizac¸ a˜ o – Compete2020 (FEDER; POCI-01-0145FEDER-016768 and POCI-01-0145-FEDER-030882). We acknowledge financial support from France Bio Imaging no. ANR-10-INBS-04-01 and ImagImm CIML imaging. We thank Noella Lopes-Pappalardo and Alexandre Boissonnas for reading the manuscript and suggestions and Lionel Spinelli for useful statistical advice. We thank Marc Barad and Sylvain Bigot from the CIML Cytometry core facility and Alice Carrier and Laurence Borge of the CRCM metabolomics core facility. We thank Pierre Golstein for mentoring and correcting the manuscript.

AUTHOR CONTRIBUTIONS

Conceptualization, R.J.A.; Method Development, R.J.A. and A.J.C.; Validation, R.J.A., A.J.C., R.C., J.-P.G., A.I.B., E.B., P.Y., and V.C.; Formal Analysis, R.J.A., A.J.C., and B.S.; Investigation, R.J.A., A.J.C., M.F.K., and P.P.; Tissue Resources, E.T., D.F.-B., S.B., and M.F.K.; Writing – Original Draft, R.J.A.; Writing, R.J.A., A.J.C., E.G., M.F.K., and P.P.; Writing – Review & Editing, R.J.A., A.J.C., E.G., E.T., R.C., M.F.K., and P.P.; Visualization, R.J.A., A.J.C., E.G., M.F.K., and P.P.; Supervision, R.J.A., M.F.K., and P.P.; Funding Acquisition, R.J.A., M.F.K., and P.P.

DECLARATION OF INTERESTS

The authors declare no competing interests. There are restrictions to the commercial use of SCENITH due to a pending patent application (PCT/EP2020/ 060486).

Received: March 18, 2020
Revised: August 9, 2020
Accepted: November 11, 2020
Published: December 1, 2020

REFERENCES

Ahl, P.J., Hopkins, R.A., Xiang, W.W., Au, B., Kaliaperumal, N., Fairhurst, A.M., and Connolly, J.E. (2020). Met-Flow, a strategy for single-cell metabolic analysis highlights dynamic changes in immune subpopulations. Commun Biol. 3, 305.

Amiel, E., Everts, B., Freitas, T.C., King, I.L., Curtis, J.D., Pearce, E.L., and Pearce, E.J. (2012). Inhibition of mechanistic target of rapamycin promotes dendritic cell activation and enhances therapeutic autologous vaccination in mice. J. Immunol. 189, 2151–2158.

Andrews, T.M., and Tata, J.R. (1971). Protein synthesis by membrane-bound and free ribosomes of secretory and non-secretory tissues. Biochem. J. 121, 683–694.

Antonia, S.J., Villegas, A., Daniel, D., Vicente, D., Murakami, S., Hui, R., Kurata, T., Chiappori, A., Lee, K.H., de Wit, M., et al.; PACIFIC Investigators (2018). Overall survival with durvalumab after chemoradiotherapy in stage III NSCLC. N. Engl. J. Med. 379, 2342–2350.

Argu€ello, R.J., Reverendo, M., Mendes, A., Camosseto, V., Torres, A.G., Ribas de Pouplana, L., van de Pavert, S.A., Gatti, E., and Pierre, P. (2018). SunRiSE measuring translation elongation at single-cell resolution by means of flow cytometry. J. Cell Sci. 131, jcs214346.

Artyomov, M.N., and Van den Bossche, J. (2020). Immunometabolism in the single-cell era. Cell Metab. 32, 710–725.

Attar, M., Sharma, E., Li, S., Bryer, C., Cubitt, L., Broxholme, J., Lockstone, H., Kinchen, J., Simmons, A., Piazza, P., et al. (2018). A practical solution for preserving single cells for RNA sequencing. Sci. Rep. 8, 2151.

Aviner, R. (2020). The science of puromycin: from studies of ribosome function to applications in biotechnology. Comput. Struct. Biotechnol. J. 18, 1074–1083.

Buck, M.D., O'Sullivan, D., and Pearce, E.L. (2015). T cell metabolism drives immunity. J. Exp. Med. 212, 1345–1360.

Buttgereit, F., and Brand, M.D. (1995). A hierarchy of ATP-consuming processes in mammalian cells. Biochem. J. 312, 163–167.

Chang, C.H., Qiu, J., O'Sullivan, D., Buck, M.D., Noguchi, T., Curtis, J.D., Chen, Q., Gindin, M., Gubin, M.M., van der Windt, G.J.W., et al. (2015). Metabolic competition in the tumor microenvironment is a driver of cancer progression. Cell 162, 1229–1241.

Dobin, A., Davis, C.A., Schlesinger, F., Drenkow, J., Zaleski, C., Jha, S., Batut, P., Chaisson, M., and Gingeras, T.R. (2013). STAR: ultrafast universal RNA-seq aligner. Bioinformatics 29, 15–21.

Everts, B., Amiel, E., van der Windt, G.J.W., Freitas, T.C., Chott, R., Yarasheski, K.E., Pearce, E.L., and Pearce, E.J. (2012). Commitment to glycolysis sustains survival of NO-producing inflammatory dendritic cells. Blood 120, 1422–1431.

Galon, J., Costes, A., Sanchez-Cabo, F., Kirilovsky, A., Mlecnik, B., LagorcePage` s, C., Tosolini, M., Camus, M., Berger, A., Wind, P., et al. (2006). Type, density, and location of immune cells within human colorectal tumors predict clinical outcome. Science 313, 1960–1964.

Hartmann, F.J., Mrdjen, D., McCaffrey, E., Glass, D.R., Greenwald, N.F., Bharadwaj, A., Khair, Z., Verberk, S.G.S., Baranski, A., Baskar, R., et al. (2020). Single-cell metabolic profiling of human cytotoxic T cells. Nat.
Biotechnol. Published online August 31, 2020. https://doi.org/10.1038/ s41587-020-0651-8.

Hidalgo San Jose, L., and Signer, R.A.J. (2019). Cell-type-specific quantification of protein synthesis in vivo. Nat. Protoc. 14, 441–460.

Kowalczyk, M.S., Tirosh, I., Heckl, D., Rao, T.N., Dixit, A., Haas, B.J., Schneider, R.K., Wagers, A.J., Ebert, B.L., and Regev, A. (2015). Single-cell RNA-seq reveals changes in cell cycle and differentiation programs upon aging of hematopoietic stem cells. Genome Res. 25, 1860–1872.

Krawczyk, C.M., Holowka, T., Sun, J., Blagih, J., Amiel, E., DeBerardinis, R.J., Cross, J.R., Jung, E., Thompson, C.B., Jones, R.G., and Pearce, E.J. (2010). Toll-like receptor-induced changes in glycolytic metabolism regulate dendritic cell activation. Blood 115, 4742–4749.

Levine, L.S., Hiam, K.J., Marquez, D.M., Tenvooren, I., Contreras, D.C., Rathmell, J.C., and Spitzer, M.H. (2020). Single-cell metabolic analysis by mass cytometry reveals distinct transitional states of CD8 T cell differentiation. bioRxiv. https://doi.org/10.1101/2020.01.21.911545.

Lindqvist, L.M., Tandoc, K., Topisirovic, I., and Furic, L. (2018). Cross-talk between protein synthesis, energy metabolism and autophagy in cancer. Curr.
Opin. Genet. Dev. 48, 104–111.

Llufrio, E.M., Wang, L., Naser, F.J., and Patti, G.J. (2018). Sorting cells alters their redox state and cellular metabolome. Redox Biol. 16, 381–387.

Macosko, E.Z., Basu, A., Satija, R., Nemesh, J., Shekhar, K., Goldman, M., Tirosh, I., Bialas, A.R., Kamitaki, N., Martersteck, E.M., et al. (2015). Highly parallel genome-wide expression profiling of individual cells using nanoliter droplets. Cell 161, 1202–1214.

Miller, A., Nagy, C., Knapp, B., Laengle, J., Ponweiser, E., Groeger, M., Starkl, P., Bergmann, M., Wagner, O., and Haschemi, A. (2017). Exploring metabolic configurations of single cells within complex tissue microenvironments. Cell Metab. 26, 788–800.e6.

Miyamoto-Sato, E., Nemoto, N., Kobayashi, K., and Yanagawa, H. (2000). Specific bonding of puromycin to full-length protein at the C-terminus.
Nucleic Acids Res. 28, 1176–1182.

Nemoto, N., Miyamoto-Sato, E., and Yanagawa, H. (1999). Fluorescence labeling of the C-terminus of proteins with a puromycin analogue in cell-free translation systems. FEBS Lett. 462, 43–46.

O'Sullivan, D., Sanin, D.E., Pearce, E.J., and Pearce, E.L. (2019). Metabolic interventions in the immune response to cancer. Nat. Rev. Immunol. 19, 324–335.

Palmer, A., Phapale, P., Chernyavsky, I., Lavigne, R., Fay, D., Tarasov, A., Kovalev, V., Fuchser, J., Nikolenko, S., Pineau, C., et al. (2017). FDR-controlled metabolite annotation for high-resolution imaging mass spectrometry. Nat. Methods 14, 57–60.

Pearce, E.L., Walsh, M.C., Cejas, P.J., Harms, G.M., Shen, H., Wang, L.-S., Jones, R.G., and Choi, Y. (2009). Enhancing CD8 T-cell memory by modulating fatty acid metabolism. Nature 460, 103–107.

Rangaraju, V., Lauterbach, M., and Schuman, E.M. (2019). Spatially stable mitochondrial compartments fuel local translation during plasticity. Cell 176, 73–84.e15.

Roos, D., and Loos, J.A. (1973). Changes in the carbohydrate metabolism of mitogenically stimulated human peripheral lymphocytes. II. Relative importance of glycolysis and oxidative phosphorylation on phytohaemagglutinin stimulation. Exp. Cell Res. 77, 127–135.

Rosenberg, A.B., Roco, C.M., Muscat, R.A., Kuchina, A., Sample, P., Yao, Z., Graybuck, L.T., Peeler, D.J., Mukherjee, S., Chen, W., et al. (2018). Single-cell profiling of the developing mouse brain and spinal cord with split-pool barcoding. Science 360, 176–182.

Russell, D.G., Huang, L., and VanderVen, B.C. (2019). Immunometabolism at the interface between macrophages and pathogens. Nat. Rev. Immunol. 19, 291–304.

Saha, S., Shalova, I.N., and Biswas, S.K. (2017). Metabolic regulation of macrophage phenotype and function. Immunol. Rev. 280, 102–111.

Satija, R., Farrell, J.A., Gennert, D., Schier, A.F., and Regev, A. (2015). Spatial reconstruction of single-cell gene expression data. Nat. Biotechnol. 33, 495–502.

Schimmel, P. (1993). GTP hydrolysis in protein synthesis: two for Tu? Science 259, 1264–1265.

Schmidt, E.K., Clavarino, G., Ceppi, M., and Pierre, P. (2009). SUnSET, a nonradioactive method to monitor protein synthesis. Nat. Methods 6, 275–277.

Seedhom, M.O., Hickman, H.D., Wei, J., David, A., and Yewdell, J.W. (2016). Protein translation activity: a new measure of host immune cell activation. J. Immunol. 197, 1498–1506.

Stuart, T., Butler, A., Hoffman, P., Hafemeister, C., Papalexi, E., Mauck, W.M.HaoY., 3rd, Stoeckius, M., Smibert, P., and Satija, R. (2019).
Comprehensive integration of single-cell data. Cell 177, 1888–1902.e21.

van der Windt, G.J.W., Everts, B., Chang, C.H., Curtis, J.D., Freitas, T.C., Amiel, E., Pearce, E.J., and Pearce, E.L. (2012). Mitochondrial respiratory capacity is a critical regulator of CD8+ T cell memory development. Immunity 36, 68–78.

van der Windt, G.J.W., O'Sullivan, D., Everts, B., Huang, S.C.C., Buck, M.D., Curtis, J.D., Chang, C.H., Smith, A.M., Ai, T., Faubert, B., et al. (2013). CD8 memory T cells have a bioenergetic advantage that underlies their rapid recall ability. Proc. Natl. Acad. Sci. USA 110, 14336–14341.

Villani, A.-C., Satija, R., Reynolds, G., Sarkizova, S., Shekhar, K., Fletcher, J., Griesbeck, M., Butler, A., Zheng, S., Lazo, S., et al. (2017). Single-cell RNA-seq reveals new types of human blood dendritic cells, monocytes, and progenitors. Science 356, 1–10.

Vitale, I., Manic, G., Coussens, L.M., Kroemer, G., and Galluzzi, L. (2019). Macrophages and metabolism in the tumor microenvironment. Cell Metab.
30, 36–50.

Warburg, O., Gawehn, K., and Geissler, A.W. (1958). [Metabolism of leukocytes]. Z. Naturforsch. B 13B, 515–516.

Wculek, S.K., Khouili, S.C., Priego, E., Heras-Murillo, I., and Sancho, D. (2019). Metabolic control of dendritic cell functions: digesting information. Front.
Immunol. 10, 775.

Wickham, H. (2009). ggplot2 - elegant graphics for data analysis (Springer).

Wieman, H.L., Wofford, J.A., and Rathmell, J.C. (2007). Cytokine stimulation promotes glucose uptake via phosphatidylinositol-3 kinase/Akt regulation of Glut1 activity and trafficking. Mol. Biol. Cell 18, 1437–1446.

Wolchok, J.D., Chiarion-Sileni, V., Gonzalez, R., Rutkowski, P., Grob, J.J., Cowey, C.L., Lao, C.D., Wagstaff, J., Schadendorf, D., Ferrucci, P.F., et al. (2017). Overall survival with combined nivolumab and ipilimumab in advanced melanoma. N. Engl. J. Med. 377, 1345–1356.

Wool, I.G., and Kurihara, K. (1967). Determination of the number of active muscle ribosomes: effect of diabetes and insulin. Proc. Natl. Acad. Sci. USA 58, 2401–2407.

Zhang, J., Nuebel, E., Wisidagama, D.R.R., Setoguchi, K., Hong, J.S., Van Horn, C.M., Imam, S.S., Vergnes, L., Malone, C.S., Koehler, C.M., and Teitell, M.A. (2012). Measuring energy metabolism in cultured cells, including human pluripotent stem cells and differentiated cells. Nat. Protoc. 7, 1068–1085.

STAR+METHODS

KEY RESOURCES TABLE

REAGENT or RESOURCE	SOURCE	IDENTIFIER
Antibodies		
Anti-human Axl Alexa Fluor 488 (Clone: 108724)	R&D Biosystems	Cat#FAB145G
Anti-human BDCA1 PE-Cy7 (Clone: L161)	Biolegend	Cat#331516
Anti-human BDCA3 FITC (Clone: AD5-14H12)	Miltenyi Biotec	Cat#130-113-317
Anti-human BDCA4 PE (Clone: 12C2)	Biolegend	Cat#354504
Anti-human CD1c PE (Clone: L161)	Biolegend	Cat#331506
Anti-human CD1c PE/Cy7 (Clone: L161)	Biolegend	Cat#331516
Anti-human CD3 BB700 (Clone: SK7)	BD Bioscience	Cat#566575
Anti-human CD3 BV711 (Clone: UCHT1)	BD Bioscience	Cat#563725
Anti-human CD3 BV510 (Clone: HIT3a)	BD Bioscience	Cat#564713
Anti-human CD4 PE-Dazzle 594 (Clone: RPA-T4)	Biolegend	Cat#300548
Anti-human CD8a BV605 (Clone: RPA-T8)	Biolegend	Cat#301040
Anti-human CD11b PE-Cy7 (Clone: ICRF44)	eBioscience	Cat#25-0118-42
Anti-human CD11c A700 (Clone: 3.9)	eBioscience	Cat#56-0116-42
Anti-human CD11c APD-R700 (Clone: 3.9)	BD Bioscience	Cat#566610
Anti-human CD11c BUV385 (Clone: B-ly6)	BD Bioscience	Cat#563797
Anti-human CD14 BUV805 (Clone: M5E2)	BD Bioscience	Cat#612902
Anti-human CD14 BV711 (Clone: M5E2)	BD Bioscience	Cat#740773
Anti-human CD14 BV711 (Clone: M5E2)	Biolegend	Cat#301838
Anti-human CD16 BV605 (Clone: 3G8)	BD Bioscience	Cat#563172
Anti-human CD16 BV605 (Clone: 3G8)	Biolgend	Cat#302040
Anti-human CD16 BV650 (Clone: 3G8)	BD Bioscience	Cat#563692
Anti-human CD16/CD32 Human TruStain FcX	Biolegend	Cat#422302
Anti-human CD19 BB700 (Clone: SJ25C1)	BD Bioscience	Cat#566396
Anti-human CD19 BV385 (Clone: HIB19)	Biolegend	Cat#302240
Anti-human CD19 BV510 (Clone: HIB19)	BD Bioscience	Cat#740164
Anti-human CD20 BB700 (Clone: 2H7)	BD Bioscience	Cat#745889
Anti-human CD20 BV785 (Clone: 2H7)	Biolegend	Cat#302355
Anti-human CD22 PE-Cy7 (Clone: HIB22)	BD Bioscience	Cat#563941
Anti-human CD25 APC (Clone: M-A251)	BD Bioscience	Cat#560987

Anti-human CD38 Alexa Fluor 488 (Clone: HIT-2)	Biolegend	Cat#303512
Anti-human CD38 APC-R700 (Clone: HIT-2)	BD Bioscience	Cat#564979
Anti-human CD38 BV786 (Clone: HIT-2)	BD Bioscience	Cat#563964
Anti-human CD44 BUV737 (Clone: G44-26)	BD Bioscience	Cat#564941
Anti-human CD45 APC-eFluor 780 (Clone: HI30)	eBioscience	Cat#47-0459-42
Anti-human CD45RA BV785 (Clone: HI100)	Biolegend	Cat#304140
Anti-human CD45RO PE (Clone: UCHL1)	Biolegend	Cat#304206
Anti-human CD56 BB700 (Clone: NCAM16.2)	BD Bioscience	Cat#566573

(Continued on next page)

Continued

REAGENT or RESOURCE	SOURCE	IDENTIFIER
Anti-human CD56 BUV737 (Clone: NCAM16.2)	BD Bioscience	Cat#612767
Anti-human CD56 BV510 (Clone: B159)	BD Bioscience	Cat#740171
Anti-human CD64 BUV737 (Clone: 10.1)	BD Biocience	Cat#564425
Anti-human CD86 BUV737 (Clone: FUN-1)	BD Bioscience	Cat#564428
Anti-human CD90 PE (Clone: 5E10)	Biolegend	Cat#328110
Anti-human CD106 PE (Clone: 51-10C9)	BD Bioscience	Cat#555647
Anti-human CD117 BV785 (Clone: 104D2)	Biolegend	Cat#313238
Anti-human CD123 BV785 (Clone: 6H6)	Biolegend	Cat#306031
Anti-human CD127 BV650 (Clone: A019D5)	Biolegend	Cat#351326
Anti-human CD141 APC (Clone: 1A4)	BD Bioscience	Cat#564123
Anti-human CD163 AF647 (Clone: GHI/61)	BD Bioscience	Cat#562669
Anti-human CD163 BV650 (Clone: GHI/61)	BD Bioscience	Cat#563888
Anti-human CD197 BV421 (Clone: G043H7)	Biolegend	Cat#353208
Anti-human CD197 PE/Dazzle 594 (Clone: G043H7)	Biolegend	Cat#353236
Anti-human CD206 FITC (Clone: 15-2)	Biolegend	Cat#321104
Anti-human CD213a1 PE/Cy7 (Clone: SS12B)	Biolegend	Cat#360407
Anti-human CD326 (Ep-CAM) BV650 (Clone: 9C6)	Biolegend	Cat#324226
Anti-human CD370/Clec9A PE (Clone: 3A4)	BD Bioscience	Cat#563488
Anti-human CTLA4 BV421 (Clone: BNI3)	Biolegend	Cat#369606
Anti-human FcεRIa BV421 (Clone: AER-37)	Biolegend	Cat#334624

Anti-human FOXP3 PE-Cy7 (Clone: PCH101)	eBiocience	Cat#25-4776-42
Anti-human HLA-DR BV605 (Clone: L243)	Biolegend	Cat#307640
Anti-human HLA-DR BUV395 (Clone: G46-6)	BD Bioscience	Cat#564040
Anti-human ICOS BV711 (Clone: DX29)	BD Bioscience	Cat#563833
Anti-human Ki67 AF488 (Clone: B56)	BD Bioscience	Cat#558616
Anti-human PD-1 BV786 (Clone: EH12)	BD Bioscience	Cat#563789
Anti-human PD-L1 BV786 (Clone: MIH1)	BD Bioscience	Cat#563739
Anti-human PD-L2 BV650 (Clone: MIH18)	BD Bioscience	Cat#563844
Anti-mouse B220 BV421 (Clone: RA3-6B2)	Biolegend	Cat#103251
Anti-mouse CD3 BV421 (Clone: 145-2C11)	Biolegend	Cat#100335
Anti-mouse CD4 APC-eFluor 780 (Clone: RM4-5)	eBioscience	Cat#47-0042-82
Anti-mouse CD8 APC (Clone: 53-6.7)	eBioscience	Cat#17-0081-33
Anti-mouse CD11c BB515 (Clone: N418)	DB Biosience	Cat#565586
Anti-mouse CD16/CD32 Mouse BD Fc Block (Clone: 2.4G2)	BD Pharmigen	Cat#553142
Anti-mouse CD44 PE (Clone: IM-7)	Biolegend	Cat#103023
Anti-mouse CD62L BV785 (Clone: MEL-14)	Biolegend	Cat#10440
Anti-mouse CD80 PerCP-Cy5.5 (Clone: 16-10A1)	Biolegend	Cat#104722
Anti-mouse Ki67 PE-eFluor-610 (Clone: SolA15)	eBioscience	Cat#61-5698-82
Anti-mouse Ly6C BV711 (Clone: HK1.4)	Biolegend	Cat#128037
Anti-mouse Ly6G PE-Cy7 (Clone: 1A8)	Biolegend	Cat#127618
Anti-mouse CD86 APC (Clone: GL1)	BD Bioscience	Cat#558703

(Continued on next page)

Continued

REAGENT or RESOURCE	SOURCE	IDENTIFIER
Anti-mouse MHC II Alexa Fluor 700 (Clone: M5/114.15.2)	eBioscience	Cat#56-5321-82
Anti-mouse MHC II BUV805 (Clone M5/ 114.15.2)	BD Bioscience	Cat#748844
Anti-mouse NK1.1 BV510 (Clone PK136)	Biolegend	Cat#108373
Anti-Puromycin Alexa Fluor 647 (Clone: R4743L-E8)	This paper	RRID: AB_2827926
Anti-Puromycin Alexa Fluor 488 (Clone: R4743L-E8)	This paper	RRID: AB_2827926

Biological Samples

Human whole blood	IFS (Institut Francais du Sang)	Cat#311
Human renal carcinoma and Juxta tumoral tissue	University of California, San Francisco (UCSF) institutional review board (IRB)approved protocol (UCSF Committee on Human Research (CHR)	Trial protocol number: 13-12246; UCSF IRB approved protocol (UCSF IRB# 14-15342)
Human meningioma	La Timone hospital. Tumor bank	Authorization number AC-2018-31053
Human brain metastasis	La Timone hospital. Tumor bank	Authorization number B-0033-00097
Chemicals, Peptides, and Recombinant Proteins		
Actinomycin D (ActD)	Merck	Cat#A1410-2MG
2-Deoxy-Glucose (2DG)	Merck	Cat#D6134-25G
B-mercaptoethanoel	VWR	Cat#0482-100ML
Cycloheximide (CHX)	Merck	Cat#01810-1G
Dimethyl sulfoxide (DMSO)	Merck	Cat#D8418-100ML
DNasel	Merck	Cat#11284932001
Extrapure LPS	Invivogen	Cat#tlrl-2216
FCCP	Merck	Cat#C2920-10MG
Gentamicin	Merck	Cat#G1272-10ML
Glucose	Merck	Cat#G7021
Harringtonine	Abcam	Cat#ab141941
Ionomycin	Merck	Cat#I-0634
L-glutamine	Life technologies	Cat#25030-024
Liberase TL research Grade	Merck	Cat#540102001
Oligomycin A	Merck	Cat#75351-5MG
PMA	Merck	Cat#P-8139
Poly I:C	Invivogen	Cat#tlrl-pic
Puromycin	Merck	Cat#P7255
Sodium pyruvate	Life Technologies	Cat#11360-039
Critical Commercial Assays		
Brilliant Stain Buffer Plus	BD Bioscience	Cat#566385
CellTiter-Glo Luminescent Cell Viability Assay	Promega	Cat#G7570
Chromium Single Cells 3^0 Library & Gel Bead Kit v2	10X genomic	Cat#120237
Chromium Single Cell A Chip Kit	10X Genomics	Cat#120236
Chromium i7 Multiplex Kit	10X Genomics	Cat#120262
Dynabeads Hum. T-Activator CD3/CD28 for T Cell Expansion and Activation	Life Technologies	Cat#11131D
Fixation/Permeabilization Solution Kit	BD Bioscience	Cat#554714

Foxp3 / Transcription Factor Staining Buffer Set	eBioscience	Cat#00-5323-00

(Continued on next page)

Continued

REAGENT or RESOURCE	SOURCE	IDENTIFIER
LIVE/DEAD Fixable Aqua Dead Cell Stain (BV510)	Thermo Fisher	Cat#L34957
RosetteSep Human T Cell Enrichment Cocktail	Stem Cell Technologies	Cat#15021
Zombie UV Fixable Viability kit	Biolegend	Cat#423107
Zombie Yellow Fixable Viability Kit	Biolegend	Cat#BLE423103
Deposited Data		
Single cell RNA-seq data	This paper	GEO: GSE159913
Experimental Models: Cell Lines		
Mouse: MEF cells	ATCC	SCRC-1008
Experimental Models: Organisms/Strains		
CellRanger (V3.02 and v3.1.0)	10X Genomics	https://support.10xgenomics.com/singlecell-gene-expression/software/downloads/ latest
Mouse: C57BL/6J	The Jackson Laboratory	Stock 000664
Software and Algorithms		
FlowJo	Treestar	V10.3
FlowR	Guillaume VOISSINE	https://github.com/VoisinneG/flowR
Ggplot2 (v3.2.1, R package)	Wickham, 2009	https://ggplot2.tidyverse.org
Seahorse Wave Desktop	Agilent	V2.6
Prism8	GraphPad	V8.3
R (v3.6.1)	Cran, The R foundation	https://www.r-project.org
R software package Seurat	Satija et al., 2015	http://satijalab.org/seurat
Seurat (v3.1.0, R package)	Stuart et al., 2019	https://github.com/satijalab/seurat

RESOURCE AVAILABILITY

Lead Contact

Further information and requests for resources and reagents should be directed to and will be fulfilled by the Lead Contact, Rafael J. Arguello (€ arguello@ciml.univ-mrs.fr).

Materials Availability

All the reagents, including a full panel of inhibitors and the monoclonal antibody clone R4743L-E8, conjugated with Alexa Fluor 647 or Alexa Fluor 488 (SCENITH kit) are available upon reasonable request. Further information by email to the lead contact and at http://www.scenith.com/.

Data and Code Availability

The accession number for the single cell RNA sequencing data reported in this paper is GEO: GSE159913 [NCBI tracking system #21365922]

EXPERIMENTAL MODEL AND SUBJECT DETAILS

Mouse Experiments

Wild type C57BL/6 mice were purchased from Jackson Laboratories and maintained in the animal facility of CIML under specific pathogen-free conditions and maintained at 21C in a 12 h light-dark cycle with water and food ad libitum. This study was carried out in strict accordance with the recommendations in the Guide for the Care and Use of Laboratory Animals the French Ministry of Agriculture and of the European Union. Animals were housed in the CIML animal facilities accredited by the French Ministry of Agriculture to perform experiments on alive mice. All animal experiments were approved by Direction De´ partementale des Services Ve´ te´ rinaires des Bouches du Rhoˆ ne (Approval number A13-543). All efforts were made to minimize animal suffering.

To obtain blood, six to eight week male mice where euthanized by CO_2 and blood was collected by cardiac puncture in Heparin tubes. To obtain splenocytes, six to eight weeks old wild type C57BL/6J male mice were euthanized by cervical dislocation and splenectomized. Mouse splenocytes were cultured in DMEM containing 5% of Fetal Calf Serum (FCS) and 50 mM of 2-Mercaptoethanol (Mouse cells culture media, MCCM) at 37C 5% of CO_2. Single cells suspentions from the spleens were generated and cultured in MCCM.

For in vitro studies, FLT3L BM-derived DCs (FLT3L-bmDCs) were differentiated in vitro from the bone marrow of 6-8 week/old from the same male mice. Bone marrow were kept from femur and tibia and plate at 1.5 3 10^6 cells/mL with 4mL/well in 6-well plates in RPMI (GIBCO), 10% of Fetal Calf Serum (FCS) and 50 mM of 2-Mercaptoethanol (Mouse cells culture media, MCCM) during 6 days at 37C 5% of CO_2 culture. Differeciation has been done by adding directly FLT3L in culture at day 0.

Human Experiments

The renal carcinoma patient enrolled in this study provided written and informed consent to tissue collection under a University of California, San Francisco (UCSF) institutional review board (IRB)-approved protocol (UCSF Committee on Human Research (CHR) no. 13-12246). The meningioma and brain meastasis patients enroled in this study provided written and informed consent in accordance with institutional, national guidelines and the Declaration of Helsinki. This protocol was approved by institutional review board (AP-HM CRB-TBM tumor bank: authorization number AC-2018-31053, B-0033-00097). The identity, age (between 30 and 60) and sex of the adult cancer patients and healthy donors was kept confidential following the ethics comitee guidelines.

Mononuclear cell enriched from blood of healthy donors (P1-P5) (3 Female, 2 Male; age between 30 and 60; mean 43) was submitted to Ficoll-paque plus (PBL Biomedical Laboratories). PBMCs and whole blood were cultured in the absense (non stimulated) or in the presence of LPS for 4 h. Immune cell stimulations were performed in the absence (Control) or presence of 0,1 mg/mL of extrapure Lipopolysacharide (Invivogen), 10 mg/mL Poly I:C (Invivogen) or PMA (5 ng/mL; Sigma) and ionomycin (500 ng/mL) over night for T cell stimulations and 4 h for DCs. T cells from human donors (P1, P2, P3) were isolated using the RosetteSep negative isolation method and activated (using BD Human T cell activator beads coated with anti-CD3 and anti-CD28) or not.

Cell Lines

Mouse Embryonic Fibroblast (MEF) cells derived from C57BL/6 background male and female sex mixed were used. For experiments, MEFs were cultured in DMEM culture media supplemented with 10% FCS at 37C 5% of CO_2 culture.

METHOD DETAILS

ATP Measurement

2 3 10^4 MEFs were seeded in 100ul of 5% FCS DMEM culture media ON in opaque 96 well plates. Cells were incubated with the inhibitors for the times indicated in the Figure. After, 100ul of Cell titer-Glo luminiscence ATP reconstituted buffer and substrate (Promega) was added to each well and Luminiscence was measured after 10 min following manufacturer instructions. A standard curve with ATP was performed using the same kit and following manufacturer instructions.

Metabolic Flux Analysis (Seahorse)

OCR and ECAR were measured with the XF24 Extracellular Flux Analyzer (Seahorse Bioscience). 4 3 10^5 cells with aCD3/aCD28 beads or not, were placed in triplicates in XF medium (nonbuffered Dulbecco's modified Eagle's medium containing 2.5 mM glucose, 2 mM L-glutamine, and 1 mM sodium pyruvate) and monitored 25 min under basal conditions and in response to 10mM glucose, 1 mM oligomycin, 100 mM 2-Deoxy-Glucose. Glycolytic capacity was measured by the difference between ECAR level after add oligomycin and before add glucose. OCR, ECAR and SRC parameters was analyzed and extract from Agilent Seahorse Wave Desktop software. Glycolytic capacity was obtained by the difference between ECAR level after add Oligomycin and before add Glucose.

SCENITH

Fifty microliters of blood were seeded in 96 well plates for studying blood cells metabolism. Alternatively cells were plated at 1 3 10^6 cells/mL, 0.5 mL/well in 48-well plates. Experimental duplicates/triplicates were performed in all conditions. After differentiation, activation or harvesting of human of cells, wells were treated during 30-45 min with Control, 2-Deoxy-D-Glucose (DG, final concentration 100mM), Oligomycin (Oligo, final concentration 1 mM), or a sequential combination of the drugs at the final concentrations before mentioned. As negative control, the translation initiation inhibitor Harringtonine was added 15 min before addition of puro (Harringtonine, 2 mg/mL). Puro (final concentration 10 mg/mL) is added during the last 15-45 min of the metabolic inhibitors treatment. After puro treatment, cells were washed in cold PBS and stained with a combination of Fc receptors blockade and fluorescent cell viability marker, then primary conjugated antibodies against surface markers during 25 min at 4C in PBS 1X 5% FCS, 2mM EDTA (FACS wash buffer). After washing, cells were fixed and permeabilized using FOXP3 fixation and permeabilization buffer (Thermofisher eBioscience) following manufacturer instructions. Intracellular staining of puro using our in house produced fluorescently labeled anti-Puro monoclonal antibody with Alexa Fluor 647 to obtain up to 10 times better signal to noise ratio than commercially available monoclonal antibodies was performed by incubating cells during 1 h at 4C diluted in permeabilization buffer. For SCENITH troubleshooting see Table S2.

Processing of Human Solid Tumors SCENITH

0.2-0.4 g of solid tumor tissue was partially dissociated using chirurgical scissors or tissue chopper (McIlwain Tissue Chopper Standard plate) to generate ''tumor explant suspention.'' Tissue explants suspention, containing tissue cubes of approximately 400 mm of cross section, were put in suspention in complete RPMI media and incubated directly with control or metabolic inhibitors, and with puro following the SCENITH protocol. Next, tumor explants were dissociated using Tissue Liberase and DNaseI with the help of a Gentle Macs (Miltenyi biotec) following manufacturers instructions. Cell suspentions were washed, counted and 2-5 3 10^6 total cells were seed in triplicates before proceeding with lived dead and FC block staining. Next, cells were stained for surface makers, fixed and permeabilized with FOXP3 fixation and permeabilization kit and stained for nuclear and cytoplasmic markers as mentioned above.

Human Single Cell RNA-sequencing

Live CD3-CD19/20-CD56- cells were sorted from renal carcinoma tumor and juxta tumoral tissue using a BD FACSAria Fusion. After sorting, cells were pelleted and resuspended at 1 3 10^3 cells/ml in 0.04% BSA/PBA and loaded onto the Chromium Controller (10X Genomics). Samples were processed for single-cell encapsulation and cDNA library generation using the Chromium Single Cell 3^0 v2 Reagent Kits (10X Genomics). The library was subsequently sequenced on an Illumina HiSeq 4000 (Illumina).

Single Cell Data Processing

Sequencing data was processed using 10X Genomics Cell Ranger V1.2 pipeline. The Cell Ranger subroutine mkfastq converted raw, Illumina bcl files to fastqs which were then passed to Cell Ranger's count, which aligned all reads using the aligner STAR (Dobin et al., 2013) against GRCh38 genomes for human cells. After filtering reads with redundant unique molecular identifiers (UMI), count generated a final gene-cellular barcode matrix. Both mkfastq and count were run with default parameters.

Cellular Identification and Clustering of scRNaseq data

For each sample, the gene - barcode matrix was passed to the R (v. 3.6.0) software package Seurat (Satija et al., 2015) (http://satijalab.org/seurat) (v3.1.1) for all downstream analyses. We then filtered on cells that expressed a minimum of 200 genes and required that all genes be expressed in at least 3 cells. We also removed cells that contained > 5% reads associated with cell cycle genes (Kowalczyk et al., 2015; Macosko et al., 2015). Count data was then log2 transformed and scaled using each cell's proportion of cell cycle genes as a nuisance factor (implemented in Seurat's ScaleData function) to correct for any remaining cell cycle effect in downstream clustering and differential expression analyses. For each sample, principal component (PC) analysis was performed on a set of highly variable genes defined by Seurat's FindVariableGenes function. Genes associated with the resulting PCs (chosen by visual inspection of scree plots) were then used for graph-based cluster identification and subsequent dimensionality reduction using t-distributed stochastic neighbor embedding (t-SNE). Cluster-based marker identification and differential expression were performed using Seurat's FindAllMarkers for all between-cluster comparisons.

QUANTIFICATION AND STATISTICAL ANALYSIS

Statistical Analysis

Statistical analysis was performed with GraphPad Prism software. When several conditions were to compare, we performed a oneway ANOVA, followed by Tukey range test to assess the significance among pairs of conditions. When only two conditions were to test, we performed Student's t test or Welch t test, according the validity of homoscedasticity hypothesis (* $p < 0.05$, ** $p < 0.01$, *** $p < 0.005$).

Quantification and Meaning of SCENITH Derived Parameters

To quantify the energetic metabolism parameters that constitute the metabolic profile of a cell, such as pathways dependency, we used simple algorithms that quantifiy the relative impact of inhibiting a given pathway compared to a complete inhibition of ATP synthesis (Figure 1F). While

SCENITH allow the use of any combination of metabolic or signaling inhibitors, herein we focused on inhibitors of glycolysis and of mitochondrial respiration to derive metabolic parameters. The percentual of glucose dependence (Gluc. dep) quantifies how much the translation levels are dependent on glucose oxidation. Gluc. dep is calculated as the difference between PS levels in 2-Deoxy-D-Glucose (DG) treated cells compared to control (Co), divided by the difference in PS upon complete inhibition of ATP synthesis (DG, first and then Oligomycin A, combined; treatment DGO) compared to control cells (Figure 1F). In a similar fashion, percentual mitochondrial dependence (Mitoc. dep) quantifies how much translation is dependent on oxydative phosphorylation. Mitoc. dep is defined as the difference in PS levels in Oligomycin A (''O,'' mitochondrial inhibitor) treated cells compared to control relative to the decreased in PS levels upon full inhibition of ATP synthesis inhibition (treatment DGO) also compared to control cells (Figure 1F). Two additional derived parameters, ''glycolytic capacity'' (Glyc. cap) and ''fatty acids and amino acids oxidation capacity'' (FAO and AAO cap) were also calculated. Glycolytic capacity is defined as the maximum capacity to sustain protein synthesis levels when mitochondrial OXPHOS is inhibited (Figure 1F; see Statistical Analysis). Conversely, FAO and AAO capacity is defined as the capacity to use fatty acids and aminoacids as sources for ATP production in the mitochondria when glucose oxidation is inhibited (Glycolysis and glucose-derived acetyl-CoA by OXPHOS) (Figures 1F and S1B). While the total level of translation correlates with the global metabolic activity of the cells, the dependency parameters underline essential cellular pathways that cannot be compensated, while ''capacity''; as the inverse of dependency, shows the maximun compensatory capacity of a subpopulation of cells to exploit alternative pathway/s when one is inhibited (Figures 1F and S1C).

For standard deviation calculation of SCENITH in different cell types of one sample (Figures 3 and 4), we followed the propagation of error that is required when the means of means are used into a formula. For standard deviation calculation:

Co = GeoMFI of anti-Puro-Fluorochrome upon Control treatment
DG = GeoMFI of anti-Puro-Fluorochrome upon 2-Deoxy-D-Glucose treatment
O = GeoMFI of anti-Puro-Fluorochrome upon Oligomycin A treatment
DGO = GeoMFI of anti-Puro-Fluorochrome upon DG+O treatment

$$\text{Glucose Dependence (Gluc: dep)} = \frac{100 \cdot (Co - DGO)}{(Co - DG)}$$

$$SD_{Glucdep} = \sqrt{\left(\frac{SD_{Co}}{Co - DGO}\right)^2 + \left(\frac{SD_{DG}}{Co - DGO}\right)^2 + \left(\frac{SD_{DGO}}{Co - DGO}\right)^2} \cdot \frac{100 \cdot (Co - DGO)}{(Co - DG)^2}$$

$$SD_{Glucdep} = \sqrt{\left(\frac{100 \cdot (DGO - DG)}{(Co - DG)^2}\right)^2 \cdot SD_{Co}^2 + \left(\frac{100 \cdot (Co - DGO)}{(Co - DG)^2}\right)^2 \cdot SD_{DG}^2 + \left(\frac{100}{Co - DG}\right)^2 \cdot SD_{DGO}^2}$$

$$\text{Mitochondrial dependence (Mitoc: dep)} = \frac{100 \cdot (Co - O)}{(Co - DGO)}$$

$$SD_{Mitodep} = \sqrt{\left(\frac{100 \cdot (DGO - O)}{(Co - DGO)^2}\right)^2 \cdot SD_{Co}^2 + \left(\frac{100}{Co - DGO}\right)^2 \cdot SD_{O}^2 + \left(\frac{100 \cdot (Co - O)}{(Co - DGO)^2}\right)^2 \cdot SD_{DGO}^2}$$

$$\text{Glycolytic capacity (Glyco: cap)} = 100 \cdot \frac{(Co - O)}{(Co - DGO)}$$

SDGlyc:cap: =vutu 100Coð$\overline{\text{DGODGO DG}_2}$Þ²3 SDCo2!ffi+sCo_____ 100DGO²3 SDO2ffi+vuut 100$\overline{\text{DGOðDG CoCo}_2}$Þ²3 SDDGO2!ffi ð

Þ ð Þ

FAOandAAOcapacityðFAOandAAOcapÞ = 100 $\frac{100}{\text{ðA ð}\frac{\text{A}}{\text{DGO}}\frac{\text{DG}}{\text{ÞÞ}}}$

SDFAOandAAOcap: =utuv 100ð$\overline{\text{DGO DG}_2}$Þ²3 SDCo2!ffi+sCo_____ 100DGO²3 SDO2ffi+uutv 100DGOð$\overline{\text{DG CoCo}_2}$Þ²3 SDDGO2!ffi ðCo

DGOÞ ð Þ